water

MDPI

Article

Defect-Engineered Carbon-Spinel Interfaces for Enhanced Periodate Activation for Bisphenol A Degradation

Bingfei Yan [1,2,†], Haochun Zang [2,†], Hao Lu [2], Haibo Li [3] and Bin Li [1,2,*]

[1] College of Water Sciences, Beijing Normal University, Beijing 100875, China; ybf201506@163.com
[2] State Key Laboratory of Environmental Criteria and Risk Assessment, Chinese Research Academy of Environmental Sciences, Beijing 100012, China; zanghch@126.com (H.Z.); lh13944236779@163.com (H.L.)
[3] Tianjin Key Laboratory of Aquatic Science and Technology, School of Environmental and Municipal Engineering, Tianjin Chengjian University, Tianjin 300384, China; lhb19850725@163.com
* Correspondence: libin0318@yeah.net
† These authors contributed equally to this work.

Abstract

Developing efficient and sustainable catalysts for advanced oxidation processes (AOPs) to remove endocrine-disrupting compounds remains a critical challenge. In this study, a defect-engineered $MnFe_2O_4$@SBC composite was synthesized by loading spinel $MnFe_2O_4$ onto sewage sludge-derived biochar (SBC) prepared at different calcination temperatures, and applied for efficient periodate (PI) activation toward bisphenol A (BPA) degradation. The catalytic performance exhibited a volcano-type dependence on calcination temperature, with $MnFe_2O_4$@SBC-750 achieving the highest BPA removal efficiency (98.6% within 30 min). Structural characterization revealed that $MnFe_2O_4$@SBC-750 possessed an optimized carbon structure with a balance between defect sites and graphitized domains. Mechanistic investigations demonstrated that multiple reactive oxygen species, including $^{\bullet}OH$, $O_2^{\bullet-}$, $IO_3^{\bullet}$ and $^1O_2$, were involved in BPA degradation. LC-MS analysis identified key transformation intermediates and proposed degradation pathways, while toxicity assessment confirmed reduced ecological risks after treatment. Density functional theory (DFT) calculations indicated that $MnFe_2O_4$@SBC significantly enhanced PI adsorption and activation by promoting interfacial electron transfer and elongating the I-O bond in IO_4^-. Notably, $MnFe_2O_4$@SBC-750 exhibited the strongest electron transfer capability, attributed to the optimal regulation of defect density and graphitization degree, which facilitated π-d electronic coupling at the $MnFe_2O_4$-SBC interface. Overall, this work elucidates the critical role of defect regulation in spinel biochar-based catalysts for oxidant activation and provides a sustainable strategy for converting sewage sludge into high-performance catalysts for water purification.

Keywords: $MnFe_2O_4$@SBC; periodate activation; advanced oxidation technology; defect engineering; π-d electronic coupling

Academic Editor: Antonio Zuorro

Received: 27 April 2026
Revised: 12 May 2026
Accepted: 18 May 2026
Published: 23 May 2026

1. Introduction

Bisphenol A (BPA) is a widely used industrial chemical that plays a significant role in the production of polycarbonate plastics and epoxy resins [1]. These materials are critical in the manufacturing of everyday products such as beverage containers, protective coatings and food packaging. Due to its chemical stability, malleability and heat resistance, BPA has been utilized extensively across various industries [2]. However, BPA is an endocrine-disrupting chemical (EDC) that poses serious health risks by interfering with hormone

regulation and disrupting endocrine functions, which leads to various health issues such as developmental and metabolic disorders [3]. The environmental impact of BPA is equally concerning, as it is highly persistent and resistant to degradation, often accumulating in water sources due to wastewater discharge from industrial processes and leaching from landfills [4]. Groundwater contamination by BPA has reached alarming levels in some regions, with concentrations exceeding 740 μg L^{-1} in certain areas affected by landfill leachates [5]. Studies have shown that even low concentrations of BPA can adversely affect aquatic organisms, including fish and invertebrates, causing developmental abnormalities and reproductive disruptions [6], as well as BPA ubiquity in human biological samples, such as urine, blood and breast milk [7]. Given these concerns, the development of advanced, cost-effective, and environmentally friendly treatment methods for BPA degradation is critical to mitigating its impact on both human health and the environment.

Advanced oxidation processes have become a promising green and environmentally friendly new technology, with periodate (PI)-based AOPs attracting increasing attention in recent years [8]. PI is a high-valent iodine oxidant featuring a redox potential of +1.60 V, excellent stability and low transportation and storage risks compared with conventional oxidants [9]. PI can generate a suite of highly reactive oxygen species (ROS), including iodyl radicals ($IO_3^{\bullet}$), hydroxyl radicals ($^{\bullet}OH$), singlet oxygen ($^1O_2$) and superoxide radicals ($O_2^{\bullet-}$), via I-O bond cleavage, enabling rapid transformation or mineralization of refractory organic pollutants [10]. However, the reaction kinetics of unactivated PI with most organic pollutants remain slow, highlighting the urgent need for efficient activation strategies [11]. Multiple activation pathways have been developed, including transition-metal catalysis, photoactivation, ultrasound, alkali activation, redox-mediated activation and heterogeneous catalysis [12]. Among these, transition-metal-based activation stands out due to its high catalytic efficiency, low energy input and potential for generating multiple ROS synergistically. Particularly, Fe- and Mn-based oxides catalysts have demonstrated remarkable performance in PI activation [13]. Xu et al. [14] demonstrated that $MnFe_2O_4$ could efficiently activate PI to generate reactive species, such as $^1O_2$, $IO_3^{\bullet}$ and $O_2^{\bullet-}$, leading to almost 100% removal of ciprofloxacin within 90 min.

Sewage sludge, a by-product of municipal wastewater treatment, is generated in tremendous quantities worldwide and contains a complex mixture of organic matter, heavy metals and pathogenic microorganisms, posing severe environmental risks if improperly disposed of [15]. Converting sewage sludge into biochar (SBC) through pyrolysis presents a sustainable and carbon-negative strategy for sludge resource utilization [16]. SBC exhibits a carbon-rich structure with abundant oxygen-containing surface functional groups, porous architecture and a considerable specific surface area, making it a versatile catalytic substrate for advanced oxidation processes [17]. Numerous studies have demonstrated that SBC can activate PI through mechanisms involving surface functional groups (-OH, -COOH, -OOH), electron-transfer mediation, defect-induced redox reactions and inherent transition-metal species originating from wastewater sludge [18,19]. However, pristine SBC often suffers from limited catalytic efficiency, insufficient redox activity, and structural instability [20]. $MnFe_2O_4$ spinel has been proven to have excellent activation ability for PI, with high reactivity, ease of recovery and environmental and economic friendliness [21]. However, nanoscale $MnFe_2O_4$ tends to aggregate and reduces the contact between surface-active sites and PI, which decreases its catalytic performance. Previous studies have shown that the combination of $MnFe_2O_4$ with biochar as a catalyst exhibits strong synergistic effects, which not only prevent the aggregation of spinel nanoparticles but also promote the generation of reactive oxygen species and enhance catalytic stability [22]. Notably, defect structures in biochar can disrupt the symmetry of the π-conjugated carbon framework and introduce unpaired electrons, thereby inducing localized charge polarization and

enhancing interfacial electron transfer [23]. For instance, Luo et al. [24] demonstrated that neighboring carbon vacancy defects could substantially reconstruct the local electronic structure, giving rise to intensified interfacial charge coupling and thereby promoting the activation of reactant molecules. However, the defect density of biochar is dependent on thermal treatment conditions, and biochar annealed at different temperatures exhibit distinct defect types and distributions [25]. These differences can directly affect the extent of π-electron delocalization, the strength of interfacial electronic coupling, and overall charge transport behavior [26]. Although previous studies have revealed the positive role of defect structures in catalytic reactions, how the regulation of defect density influences the electronic structure of the carbon support–metal interface and the overall catalytic performance of the system remains insufficiently understood. To our knowledge, no prior studies have comprehensively elucidated the impact of defect density modulation on catalyst-wide electronic interactions and reactivity.

Therefore, in this study, municipal sewage sludge was employed as the precursor to prepare a series of defect-engineered SBC via pyrolysis at different temperatures, which were further loaded with $MnFe_2O_4$ to construct $MnFe_2O_4$@SBC composite catalysts. The removal efficiency and degradation mechanism of BPA were systematically investigated through structural characterization, reactive species identification, and kinetic analyses. In combination with density functional theory (DFT) calculations, the regulatory effects of SBC defect density and graphitization degree at different calcination temperatures on the interfacial electronic structure of $MnFe_2O_4$@SBC, as well as on PI adsorption and activation behavior, were elucidated. The results demonstrate that the synergistic interplay between defect density and π-d electronic coupling plays a decisive role in determining the catalytic activity. This work provides important theoretical insights into the defect engineering of carbon-based composite catalysts for enhanced catalytic performance.

2. Materials and Methods

2.1. Materials and Synthesis of Catalysts

Details of these chemicals and reagents can be found in Supplementary Materials Text S1. The raw sewage sludge was collected from the Hedong Sludge Treatment Plant (Beijing, China). Typically, the sludge was first cleaned three times with deionized water (DI water) in an ultrasonic cleaning machine. After natural sedimentation, the sludge was dried in an oil bath at 105 °C until a constant weight was achieved. It was then ground and sieved through a 60-mesh screen to obtain the biochar precursor. The precursor was then pyrolyzed in a tube furnace at a specified temperature with a heating rate of 5 °C min^{-1} for 2 h, under a nitrogen flow of 300 mL L^{-1}. After natural cooling, the biochar produced from the pyrolysis was washed repeatedly with ethanol and DI water, and then dried at 60 °C for 12 h to obtain SBC. The $MnFe_2O_4$@SBC catalyst was further synthesized by hydrothermal treatment. First, 0.095 g of Manganese chloride tetrahydrate ($MnCl_2 \cdot 4H_2O$, 12 mM), 0.399 g of Ferric nitrate nonahydrate ($Fe(NO_3)_3 \cdot 9H_2O$, 24 mM) (molar ratio of Mn:Fe = 1:2) and 0.6 g of SBC were dissolved in 40 mL of DI water and stirred magnetically for 30 min. The resulting mixture was aged at room temperature for 4 h, and then transferred to a Teflon-lined stainless-steel autoclave for hydrothermal treatment at 180 °C for 12 h. After cooling to room temperature, the product was carefully washed with deionized water and dried in an oven at 60 °C to obtain $MnFe_2O_4$@SBC. Additionally, $MnFe_2O_4$ was prepared following the same procedure but without adding SBC.

2.2. Experimental Procedures

Unless otherwise specified, all degradation experiments were conducted in a 100 mL beaker at 25 ± 1 °C with a stirring speed of 350 rpm. First, the BPA stock solution

(100 mg L^{-1}) was diluted to the target concentration with DI water in the beaker and stirred to ensure uniform mixing. Subsequently, a certain amount of $MnFe_2O_4$@SBC was added to the system to initiate the adsorption process. After equilibrium was reached (30 min), 1 mL of the mixed solution was withdrawn using a syringe and filtered through a 0.22 μm Polytetrafluoroethylene (PTFE) filter membrane. PI stock solution (200 mM) was then immediately added to trigger the catalytic reaction. Samples were taken at specific time points (2, 5, 10, 15, 20 and 30 min), filtered through a 0.22 μm membrane, and immediately treated with 100 μL of 0.1 M sodium thiosulfate ($Na_2S_2O_3$, 100 mM) solution to remove any remaining PI and reactive species. All experiments were repeated at least three times to obtain the standard deviation. BPA was quantitatively analyzed using a high-performance liquid chromatography (HPLC, Agilent Technologies Inc., Braum, Germany) equipped with a C18 reverse-phase column and UV detector at 278 nm. Additional experimental procedures are provided in Text S2.

2.3. Analytical Methods

The quantification of PI, iodinated toxic by-products and other organic pollutants was performed using HPLC. Detailed HPLC testing methods were provided in Table S1. I_2 and I_3^- were identified using the starch colorimetric method. Reactive free radicals were identified by electron paramagnetic resonance (EPR, Bruker Magnetic Resonance, Saarbrücken, Germany), with DMPO used as a spin trap to detect the generated $^{\bullet}OH$, $O_2^{\bullet-}$ and $IO_3^{\bullet}$ in the $MnFe_2O_4$@SBC/PI system, and TEMP used as a spin trap for the non-radical $^1O_2$. Intermediate products of BPA degradation were analyzed using ultra-performance liquid chromatography–mass spectrometry (UPLC-MS, Thermo Fisher Scientific, Waltham, MA, USA). The toxicity of BPA and its intermediate degradation products was assessed using the Toxicity Estimation Software Tool (T.E.S.T., v5.1.2) by the U.S. Environmental Protection Agency (EPA). Additional characterization methods and instrument parameters are provided in Text S3, and the analytical methods are detailed in Text S4.

2.4. Theoretical Calculations

DFT calculations were performed using the Vienna ab initio simulation package (VASP.5.4.4) and Gaussian 16. The detailed computational procedures and parameters were provided in Text S5.

3. Results and Discussions

3.1. Catalyst Characterization

The surface morphology of SBC, $MnFe_2O_4$ and $MnFe_2O_4$@SBC was investigated by scanning electron microscope (SEM). As shown in Figure 1a,d, SBC exhibited a relatively flat surface with occasional block-like and sheet-like regions. EDS analysis revealed that SBC contained abundant C and O, along with Mn and Fe (Figure S1a). However, these Mn and Fe containing species originated from the complex metal matrix inherent to municipal sludge and were transformed into poorly soluble oxides or silicate-bound phases during pyrolysis at 550 °C. Such thermally stabilized forms did not dissolve or participate in the subsequent hydrothermal synthesis. The synthesized $MnFe_2O_4$ sample displayed nano-sized granular particles with aggregation, and its EDS spectrum confirmed the presence of O, Mn and Fe (Figures 1b,e and S1b). The SEM images of $MnFe_2O_4$@SBC showed that $MnFe_2O_4$ nanoparticles and small clusters are attached to the surface of the biochar, indicating that the carbon matrix effectively inhibited the particle agglomeration commonly observed in pure $MnFe_2O_4$ (Figure 1c,f). Elemental mapping of $MnFe_2O_4$@SBC (Figure S1c) revealed homogeneous distributions of C, O, Mn and Fe, confirming that $MnFe_2O_4$ has been successfully loaded onto SBC. Transmission electron microscope (TEM) images further

confirmed the spinel nanostructure of $MnFe_2O_4$@SBC on the surface (Figure 1g). High-resolution transmission electron microscope (HRTEM) characterization of $MnFe_2O_4$@SBC displayed lattice fringes with an interplanar spacing of approximately 0.261 nm (Figure 1h), consistent with the (311) plane of spinel $MnFe_2O_4$ [14]. In addition, selected area electron diffraction (SAED) pattern (Figure 1i) displayed clear diffraction rings corresponding to the (311) lattice plane of $MnFe_2O_4$ [27].

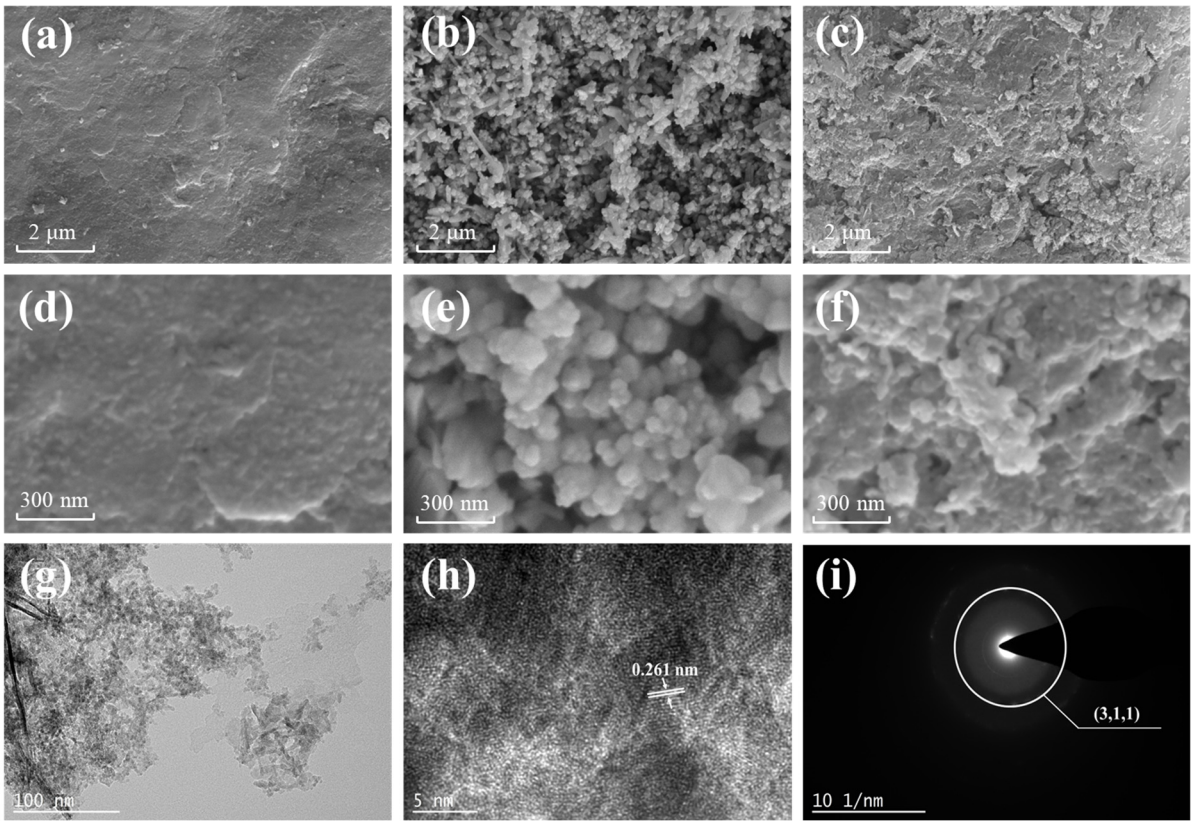

Figure 1. SEM images of 2 μm and 300 nm for (**a**,**d**) SBC, (**b**,**e**) $MnFe_2O_4$ and (**c**,**f**) $MnFe_2O_4$@SBC, (**g**) TEM and (**h**,**i**) HR-TEM images of $MnFe_2O_4$@SBC.

The surface area and pore structure of $MnFe_2O_4$@SBC were analyzed using N_2 adsorption–desorption isotherms and pore size distribution analysis. As shown in Figure S2a and Table S2, SBC exhibited a specific surface area of 86.09 m^2/g, with an average pore diameter of 8.57 nm. The specific surface area of $MnFe_2O_4$ is 27.50 m^2/g, with an average pore diameter of 18.20 nm (Figure S2b). The pore size distribution was irregular and variability. In comparison, the $MnFe_2O_4$@SBC composite exhibited a substantial increase in surface area, reaching 248.70 m^2/g and an average pore diameter of 10.76 nm (Figure S2c). This substantial increase in surface area could be attributed to the synergistic effect between $MnFe_2O_4$ nanoparticles and the biochar matrix, which enhanced the overall porosity and facilitates greater exposure of active sites. The N_2 adsorption–desorption isotherm of the composite shows a type IV adsorption isotherm with a H3 hysteresis loop [28]. Furthermore, the pore size distribution revealed that the $MnFe_2O_4$@SBC composite exhibits a well-developed pore structure with a predominant pore volume in the 10–20 nm range. The results indicated the presence of micropores and mesopores, which were beneficial for facilitating the transport of pollutants and reactive species.

The X-ray diffraction (XRD) patterns of $MnFe_2O_4$@SBC were recorded to investigate the crystallographic structure of the composite material. As shown in Figure 2a, the unique characteristic peak of $MnFe_2O_4$@SBC is assigned to the (002) plane of a hexagonal graphite

structure (JCPDS No. 99-0057), which is due to the low loading of $MnFe_2O_4$ [29]. The XRD pattern of $MnFe_2O_4$ presents several prominent diffraction peaks, which are consistent with those of spinel-type $MnFe_2O_4$ (JCPDS No. 38-0430), confirming the successful synthesis of $MnFe_2O_4$ [30]. The diffraction peaks observed at 2θ = 29.6°, 34.8°, 42.3°, 56.0° and 61.5° correspond to the (202), (311), (004), (333) and (440) crystallographic planes of $MnFe_2O_4$, respectively. The average crystallite size of $MnFe_2O_4$ calculated from the Scherrer equation using the (311) diffraction peak was approximately 17.6 nm, indicating the formation of nanosized spinel $MnFe_2O_4$ particles on the SBC surface. The relatively small crystallite size could expose more active sites and facilitate interfacial catalytic reactions during PI activation. Additionally, the XRD pattern showed characteristic peaks at 24.1°, 33.2°, 35.6°, 39.3°, 40.9°, 43.5°, 49.5° and 54.1°, which correspond to the (012), (104), (110), (006), (113), (202), (024) and (116) planes of Fe_2O_3 (JCPDS No. 87-1166) [31]. These results indicate that $MnFe_2O_4$ was successfully loaded onto SBC and that a small amount of Fe_2O_3 was generated during the synthesis process.

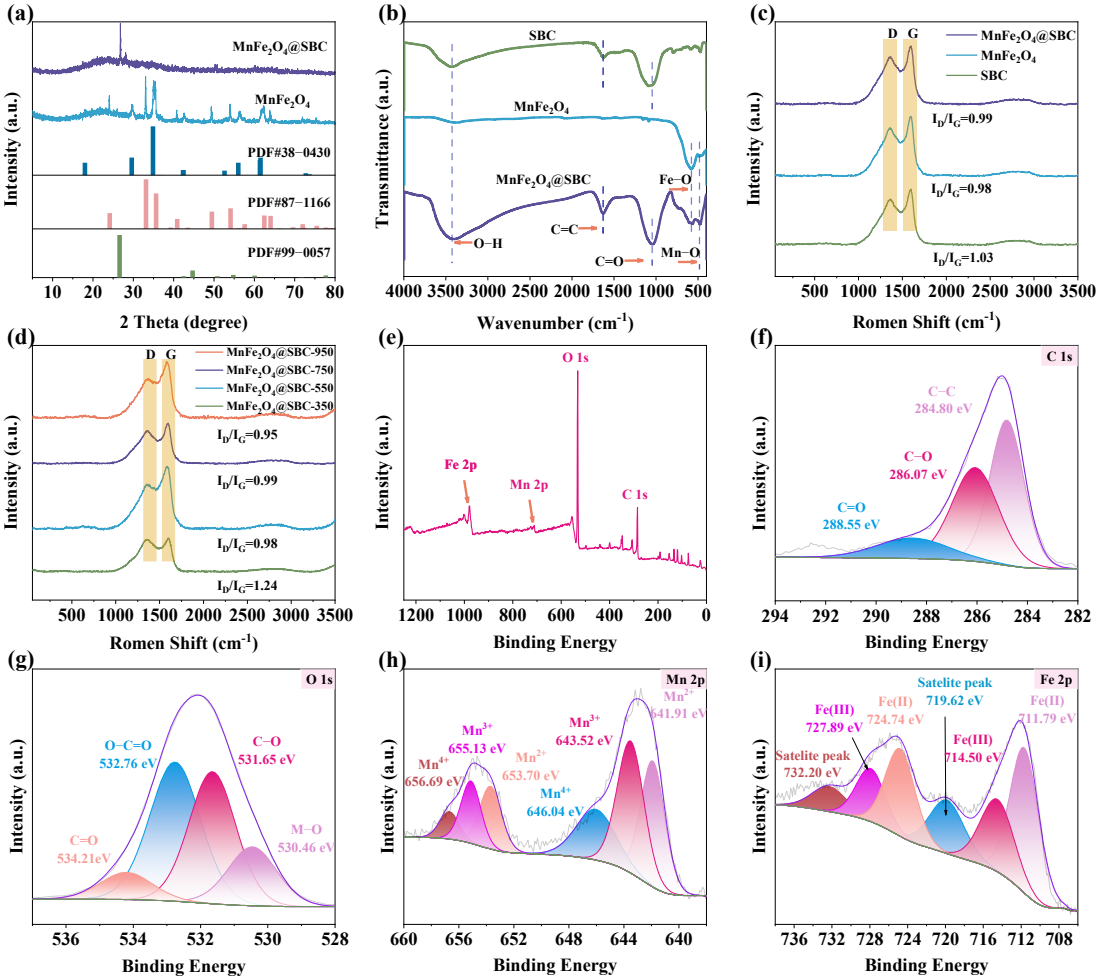

Figure 2. (**a**) XRD patterns, (**b**) FT-IR spectra and (**c**) Raman spectra of SBC, $MnFe_2O_4$ and $MnFe_2O_4$@SBC, (**d**) Raman spectra of $MnFe_2O_4$@SBC synthesized from SBC prepared at different pyrolysis temperatures, (**e**) XPS spectra of $MnFe_2O_4$@SBC, high-resolution XPS spectra of (**f**) C1s, (**g**) O1s (**h**) Mn2p and (**i**) Fe2p of $MnFe_2O_4$@SBC.

The Fourier-transform infrared (FTIR) spectra of $MnFe_2O_4$@SBC are shown in Figure 2b, providing qualitative information on the characteristic peaks of various functional groups. A prominent peak at 3415 cm^{-1} was observed, which is attributed to the O-H stretching vibration of hydroxyl groups, indicating the presence of surface hydroxyl

functionalities on SBC, $MnFe_2O_4$ and $MnFe_2O_4$@SBC [32]. At 1627 cm^{-1}, the peak corresponds to the C=C stretching vibration of the graphitic structure within SBC matrix, reflecting the aromatic nature of the material [33]. A peak at 1043 cm^{-1} was observed related to the C=O stretching vibration of carbonyl groups, likely linked to surface oxygen-containing groups [34]. The absorption bands at 584 cm^{-1} and 482 cm^{-1} in $MnFe_2O_4$ and $MnFe_2O_4$@SBC are attributed to the stretching vibrations of the Fe-O and Mn/Fe-O bonds, respectively [35]. These peaks confirm the presence of metal-oxide bonds, further supporting the successful incorporation of $MnFe_2O_4$ nanoparticles into the biochar matrix.

Raman spectroscopy was employed to further investigate the graphitization degree and structural properties of $MnFe_2O_4$@SBC. As shown in Figure 2c, the Raman spectra of SBC, $MnFe_2O_4$ and $MnFe_2O_4$@SBC exhibited two prominent peaks. The D band at 1339 cm^{-1} corresponds to defects and disordered carbon atoms, and the G band at 1590 cm^{-1} corresponds to the stretching vibration of sp^2 hybridized carbon atoms in graphite [36]. For $MnFe_2O_4$@SBC, the I_D/I_G ratio was 0.99, which is slightly higher than $MnFe_2O_4$ (I_D/I_G = 0.98) and significantly lower than SBC (I_D/I_G = 1.03). The decrease in the I_D/I_G ratio for $MnFe_2O_4$@SBC indicates a reduction in disorder and structural defects compared to SBC, which improved the material catalytic performance [35]. In addition, high degree of graphitization in $MnFe_2O_4$@SBC facilitated the exposure of active sites on the catalyst surface [37]. The structural defects and degree of graphitization of $MnFe_2O_4$@SBC prepared at different calcination temperatures were also evaluated. As shown in Figure 2d, the I_D/I_G value decreased from 1.24 for $MnFe_2O_4$@SBC-350 to 0.98 for $MnFe_2O_4$@SBC-550, indicating that increasing the calcination temperature enhanced graphitization of the carbon framework. Interestingly, the I_D/I_G value slightly increased to 0.99 for $MnFe_2O_4$@SBC-750, suggesting the generation of additional edge defects and structural regulation during the carbon reconstruction process [26]. When the calcination temperature further increased to 950 °C, the I_D/I_G value decreased to 0.95, indicating that excessive thermal treatment promoted the formation of ordered sp^2 carbon structures. Notably, $MnFe_2O_4$@SBC-750 maintained a relatively high defect density while simultaneously developing an extended π-conjugated structure. This structural feature is favorable for enhancing interfacial π-d electronic coupling with $MnFe_2O_4$, thereby facilitating electron transfer and promoting PI activation (discussed in Section 3.4).

The surface chemical states of $MnFe_2O_4$@SBC were examined through XPS. As shown in Figure 2e, the XPS survey spectrum showed clear signals of C, O, Mn and Fe, which was consistent with the expected composition of $MnFe_2O_4$@SBC. The C 1s spectrum displayed four deconvoluted peaks at 284.80 eV (C-C), 286.58 eV (C-O), 288.23 eV (C=O) and 290.51 eV (O-C=O), suggesting that oxygen-containing groups remained abundant on the composite surface (Figure 2f) [38,39]. The O 1s spectrum showed characteristic peaks at 530.00 eV, corresponding to lattice oxygen species such as Mn-O and Fe-O, while peaks at 531.63 eV, 533.34 eV and 535.04 eV were assigned to C-O, O-C=O and C=O, respectively (Figure 2g) [39,40]. The results were consistent with the findings from the XRD and FTIR analyses. The coexistence of lattice oxygen and surface oxygenated groups implied that the biochar support influenced the coordination environment of Mn and Fe, thereby enhancing the surface reactivity. The Mn 2p spectrum contained three Mn 2p3/2 peaks at 641.66 eV (Mn^{2+}), 643.94 eV (Mn^{3+}) and 646.23 eV (Mn^{4+}) (Figure 2h). Several peaks between 652 and 658 eV corresponded to Mn 2p1/2 [41,42]. The simultaneous presence of Mn^{2+}, Mn^{3+} and Mn^{4+} suggested a mixed-valence Mn environment, which was attributed to facilitate rapid electron exchange. The Fe 2p spectrum further supported the mixed-valence nature of the composite. Peaks at 711.79 eV (Fe^{2+} 2p3/2) and 714.50 eV (Fe^{3+} 2p3/2) were observed, along with a satellite peak at 719.62 eV (Figure 2i) [28]. The Fe 2p1/2 region presented peaks at 724.74 eV (Fe^{2+}), 727.78 eV (Fe^{3+}), and 731.16 eV for the satellite feature. The

coexistence of Fe^{2+} and Fe^{3+} indicated that Fe sites could participate in redox cycling, which is essential for sustaining catalytic activity. Additionally, the XPS analysis of SBC was presented in Text S6. Compared with $MnFe_2O_4$@SBC, pristine SBC exhibited weaker Fe signals, and the Mn 2p spectrum could not be reliably deconvoluted due to the low Mn content. The metal species in SBC were mainly present as dispersed and less-defined oxides. In contrast, $MnFe_2O_4$@SBC displayed significantly enhanced Mn and Fe signals with well-resolved mixed-valence states, indicating the formation of well-defined $MnFe_2O_4$ phases and a reconstructed coordination environment.

3.2. Catalytic Performance Towards BPA Removal

The effect of different $MnFe_2O_4$: SBC ratios on BPA degradation was studied to evaluate the catalytic performance of the $MnFe_2O_4$@SBC system (Figures 3a and S3a). At a 1:1 $MnFe_2O_4$:SBC ratio, the system achieved the highest catalytic efficiency, with a BPA removal rate of 98.8% (k_{obs} = 0.147 min^{-1}). When the ratio increased to 1:3, the BPA removal rate slightly decreased to 98.6%, with a k_{obs} value of 0.136 min^{-1}. Further increasing the SBC content to 1:5 resulted in a slight decrease in BPA removal efficiency to 97.8%, with a corresponding k_{obs} of 0.133 min^{-1}. The results indicated that although the system experienced a slight decline in performance, it still maintained high catalytic potential. At a 1:7 ratio, the BPA removal rate dropped to 88.3%, with a k_{obs} of 0.064 min^{-1}. At a 1:9 and 1:11 ratio, the removal efficiency further decreased to 83.1% and 69.1%, and the k_{obs} was reduced to 0.052 min^{-1} and 0.033 min^{-1}. These findings suggested that while increasing the SBC content improved the structural stability of the catalyst, an excessively low $MnFe_2O_4$: SBC ratio resulted in insufficient surface-active sites. Therefore, a $MnFe_2O_4$:SBC ratio of 1:3 was selected as the optimal catalyst, as it provided sufficient active sites for efficient PI activation and maximized BPA degradation efficiency.

The BPA degradation efficiency was evaluated using $MnFe_2O_4$@SBC catalysts prepared from SBC calcined at different temperatures (Figures 3b and S3b). $MnFe_2O_4$@SBC-350, $MnFe_2O_4$@SBC-550, and $MnFe_2O_4$@SBC-750 removed 58.3%, 77.7% and 98.6% of BPA in solution within 30 min, respectively, with corresponding k_{obs} values of 0.024 min^{-1}, 0.048 min^{-1} and 0.136 min^{-1}. These results indicated that increasing the calcination temperature promoted the formation of more ordered sp^2 carbon structures, which facilitated interfacial electron transfer between the carbon framework and $MnFe_2O_4$ [43]. Notably, $MnFe_2O_4$@SBC-750 exhibited the highest degradation efficiency, which was attributed to the coexistence of abundant defect sites and a relatively developed graphitic structure. However, the BPA degradation efficiency in the $MnFe_2O_4$@SBC-950/PI system decreased to 85.8% (k_{obs} = 0.064 min^{-1}), indicating that excessively high pyrolysis temperatures led to over-graphitization, thereby weakening the surface reactivity. Therefore, $MnFe_2O_4$@SBC-750 was selected for further investigation.

The degradation performance of BPA by $MnFe_2O_4$@SBC/PI, $MnFe_2O_4$/PI, SBC/PI and PI alone was compared to assess the catalytic efficiency of the different systems. To avoid exaggerating the degradation efficiency of the catalytic process, a 30 min pre-adsorption (without PI addition) was performed. The results showed that BPA removal through adsorption in all systems did not exceed 15%, indicating that the contribution of the adsorption process to pollutant removal was limited. As illustrated in Figures 3c and S3c, The $MnFe_2O_4$@SBC/PI system demonstrated the highest degradation efficiency, with a BPA removal rate of 98.6% and a corresponding pseudo-first-order kinetics (k_{obs}) constant of 0.136 min^{-1}. In contrast, the $MnFe_2O_4$/PI and SBC/PI systems showed lower degradation rates, with values of approximately 28.8% (k_{obs} = 0.010 min^{-1}) and 21.7% (k_{obs} = 0.006 min^{-1}), respectively. Notably, the PI-only system exhibited negligible removal, confirming that PI alone has limited degradation capability for BPA. The results

indicated that $MnFe_2O_4$@SBC exhibits significantly superior catalytic performance for PI activation compared to other systems. Moreover, Text S7 analyzed the effects of catalyst dosage, PI concentration, BPA concentration and initial pH on the BPA removal efficiency of the $MnFe_2O_4$@SBC/PI system. Considering catalytic activity and PI activation efficiency, the optimal conditions selected were [$MnFe_2O_4$@SBC] = 0.4 g L^{-1}, [BPA] = 20 mg L^{-1}, [PI] = 0.5 mM, and an initial pH of 7.

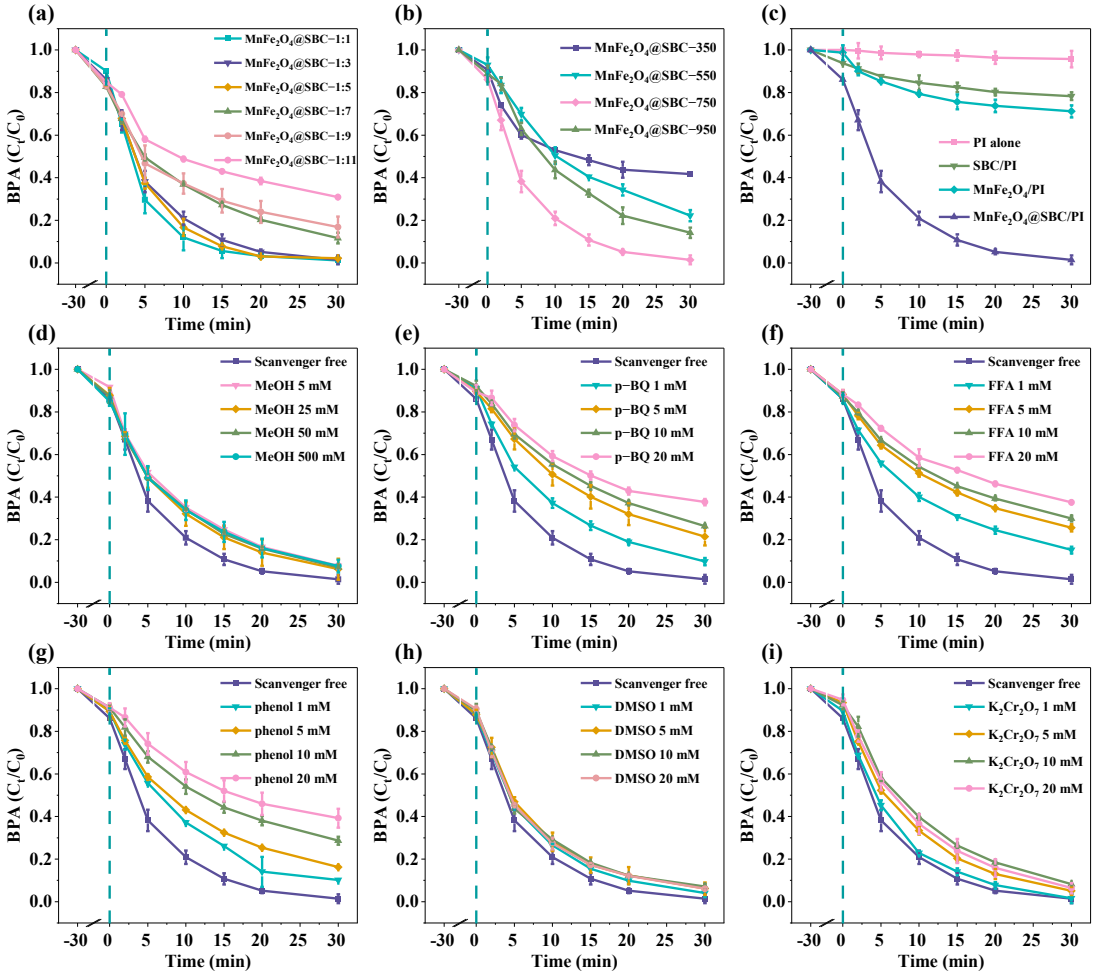

Figure 3. (**a**) Effect of $MnFe_2O_4$ loading ratio on the BPA degradation performance of $MnFe_2O_4$@SBC, (**b**) effect of calcination temperature on the catalytic performance of $MnFe_2O_4$@SBC, (**c**) comparison of BPA removal efficiency in different systems, effect of different quenchers on BPA degradation in the $MnFe_2O_4$@SBC/PI system, including (**d**) MeOH, (**e**) p-BQ, (**f**) FFA, (**g**) phenol, (**h**) DMSO and (**i**) $K_2Cr_2O_7$.

3.3. Identification of ROS

To clarify the reactive species responsible for BPA degradation in the $MnFe_2O_4$@SBC/PI system, a series of quenching experiments was conducted using different scavengers at varied concentrations. Methanol (MeOH) (k_{obs} = (3.8–7.6) × 10^8 M^{-1} s^{-1}) can be an •OH quencher [44]. As shown in Figures 3d and S4a, the addition of 5–500 mM MeOH caused only slight decrease in BPA removal (92.3–96.7%), with k_{obs} ranging from 0.087 to 0.079 min^{-1}, indicating that •OH contributed minimally to the oxidation process. p-Benzoquinone (p-BQ) was introduced to examine the contribution of $O_2^{\bullet-}$ in the reaction system (k_{obs} = (0.9–1.0) × 10^9 $M^{-1}s^{-1}$) [45]. With p-BQ concentrations of 1, 5, 10 and 20 mM, BPA removal decreased to 90.2%, 78.5%, 73.6% and 62.3%, with k_{obs} of 0.073, 0.048, 0.042 and 0.031 min^{-1}, suggesting that $O_2^{\bullet-}$ played a significant role in BPA degradation

(Figures 3e and S4b). Furfuryl alcohol (FFA) preferentially scavenges $^1O_2$ in the system (k_{obs} = 1.2 × 10^8 M^{-1} s^{-1}) [46]. The results showed that FFA also suppressed BPA degradation, with removal efficiencies dropping from 98.6% to 62.5% and k_{obs} decreasing from 0.136 to 0.029 min^{-1} as the FFA concentration increased, confirming the participation of $^1O_2$ (Figures 3f and S4c). Notably, the quenching effect of FFA on $^1O_2$ may be overestimated, because FFA can directly consume PI through an electron-transfer reaction. Therefore, FFA was used in place of BPA to examine the possible competitive consumption of PI in the system. As shown in Figure S5, the PI concentration remained unchanged in the presence of 20 mM FFA, indicating that PI consumption by FFA was negligible. Phenol was selected as the quenching agent for $IO_3^•$, and its addition markedly inhibited the removal of BPA (k_{obs} = 1.0 × 10^9 M^{-1} s^{-1}) [47]. BPA removal rate decreased from 98.6% (k_{obs} = 0.136 min^{-1}) to 89.8% (k_{obs} = 0.076 min^{-1}), 83.9% (k_{obs} = 0.067 min^{-1}), 71.3% (k_{obs} = 0.039 min^{-1}) and 60.7% (k_{obs} = 0.029 min^{-1}) when phenol concentrations increased from 0 mM to 1 mM, 5 mM, 10mM and 20 mM, respectively, indicating that $IO_3^•$ was one of the dominant reactive species in this system (Figures 3g and S4d). 2,4,6-TCP was employed as a target contaminant to further verify the contribution of $IO_3^•$ in the $MnFe_2O_4$@SBC/PI system, because $IO_3^•$ is unable to oxidize 2,4,6-TCP. The degradation efficiency of 2,4,6-TCP reached 52.7% within 14 min, confirming the presence of $IO_3^•$ in the $MnFe_2O_4$@SBC/PI system (Figure S6). Since SBC contains multiple metals and supports $MnFe_2O_4$, dimethyl sulfoxide (DMSO) was employed to exclude the possible involvement of high-valent metal-oxo species. BPA degradation remained above 90%, demonstrating that high-valent metal-oxo species were not involved (Figures 3h and S4e). $K_2Cr_2O_7$ was employed as an electron scavenger to determine whether ROS generation in the system involves solution phase electron transfer pathways [48]. As shown in Figures 3i and S4f, $K_2Cr_2O_7$ caused negligible inhibition of BPA concentration, with BPA removal efficiencies of 91.7–98.4% and k_{obs} values of 0.081–0.131 min^{-1}, suggesting that the active sites on the catalyst surface directly activate the adsorbed PI to generate ROS. The premixing experiment was used to identify ROS generation. When $MnFe_2O_4$@SBC and PI were premixed for 5, 10 and 20 min before BPA addition, the BPA removal efficiencies decreased to 62.3%, 42.4% and 19.2%, respectively (Figure S7). These results indicated that with increasing premixing time, the ROS produced in the system underwent self-quenching and were no longer available to effectively degrade BPA. Electrochemical measurements were employed to examine whether a direct electron-transfer pathway existed in the $MnFe_2O_4$@SBC/PI system. The results demonstrated that BPA did not transfer electrons to IO_4^- via the catalyst surface, indicating that a direct electron-transfer process was absent (Text S8).

EPR spectroscopy, using 5,5-dimethyl-1-pyrroline-N-oxide (DMPO) and 2,2,6,6-tetramethylpiperidine (TEMP) as spin-trapping agents, was performed to identify the ROS generated in the $MnFe_2O_4$@SBC/PI system (Figure 4). No EPR signals were detected in either the $MnFe_2O_4$@SBC or PI-only systems, confirming that neither component produced measurable radicals in isolation. As expected, when $MnFe_2O_4$@SBC was coupled with PI, distinct EPR signals were observed. At 5 min of reaction, DMPO-$^•$OH, DMPO-$O_2^{•-}$ and DMPO-$IO_3^•$ were detected. These signals became more pronounced at 10 min, demonstrating sustained radical generation within the system (Figure 4a–c). Specifically, the DMPO-$^•$OH signal showed a characteristic quartet pattern (1:2:2:1), while the DMPO-$O_2^{•-}$ signal appeared as a quartet with a 1:1:1:1 intensity ratio [45,49]. The DMPO-$IO_3^•$ adduct exhibited a signal consistent with a quartet (2:2:1:2:1:2), confirming the generation of $IO_3^•$ in the reaction [47]. Furthermore, TEMP was used to capture $^1O_2$. A distinct three-line EPR signal with a 1:1:1 intensity ratio (TEMP-$^1O_2$) appeared at 5 min and the signal intensity increased at 10 min, indicating that $^1O_2$ was generated during the reaction (Figure 4d) [50]. Upon adding BPA to the system, a noticeable decrease in signal intensity was observed

for all four signals, indicating that the primary reactive species in the $MnFe_2O_4$@SBC/PI system were $^{\bullet}OH$, $O_2^{\bullet-}$, $IO_3^{\bullet}$ and $^1O_2$.

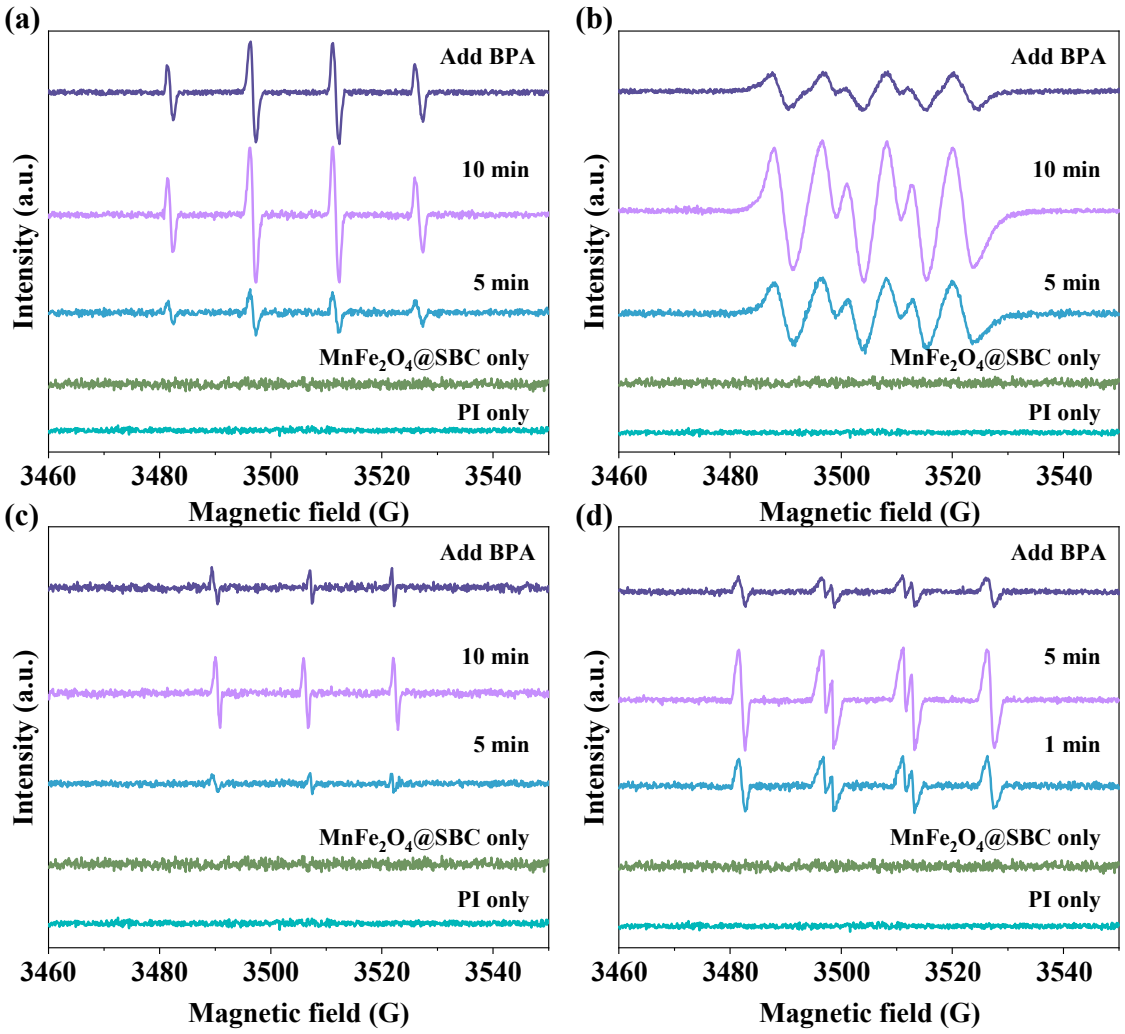

Figure 4. EPR spectra of (**a**) DMPO-$^{\bullet}OH$, (**b**) DMPO-$O_2^{\bullet-}$, (**c**) TEMP-$^1O_2$ and (**d**) DMPO-$IO_3^{\bullet}$ in PI alone, $MnFe_2O_4$@SBC alone, $MnFe_2O_4$@SBC/PI and $MnFe_2O_4$@SBC/PI with BPA.

3.4. Catalytic Mechanism of $MnFe_2O_4$@SBC

The XPS analysis was employed to investigate the changes in chemical bonds and functional groups on the $MnFe_2O_4$@SBC surface before and after the reaction (Figure S8). The C1s spectrum showed that before the reaction, the relative contents of C-C, C-O, and C=O were 46.0%, 40.4% and 13.6%, respectively. After the reaction, the relative content of these peaks shifted slightly to 46.6%, 41.0% and 12.4%, respectively. These results suggested that while the surface carbon structure remained largely unchanged, there was a shift in the carbon bonding environment, possibly due to the adsorption of reaction intermediates or surface oxidation during the catalytic process. The O1s spectrum (Figure S8a) showed that before the reaction, the relative contents of surface oxygen species C-O, O-C=O, and C=O were 35.2%, 40.3% and 8.1%, respectively. After the reaction, the relative content of C-O and O-C=O increased slightly to 38.6% and 42.1%, respectively, while the content of C=O remained. Notably, the M-O peak decreased from 16.4% to 10.7%, suggesting that M-O was a potential active site for PI activation. The Mn 2p spectra revealed that before the reaction, the Mn species were distributed as Mn^{2+} (37.7%), Mn^{3+} (40.8%) and Mn^{4+} (21.5%) (Figure S8b). After the reaction, the Mn^{2+} content increased to 39.6%, while the Mn^{3+} content decreased to 36.0%. In contrast, the Mn^{4+} content increased to 28.4%.

Similarly, the relative content of Fe^{2+} and Fe^{3+} was 50.2% and 29.7% before the reaction, respectively (Figure S8c,d). After the reaction, the content of Fe^{2+} decreased to 36.6%, while Fe^{3+} increased to 45.5%. These changes suggested that during the catalytic degradation process, Mn^{2+} (Fe^{2+}) and Mn^{3+} (Fe^{3+}) were involved in the redox cycling, leading to the interconversion of Mn species. The oxidation of Mn^{2+} to Mn^{3+} and Mn^{4+}, as well as the oxidation of Fe^{2+} to Fe^{3+}, facilitated the generation of ROS. However, the slight increase in Mn^{2+} content after the reaction was due to the regeneration of Mn^{2+} from Mn^{3+} through reaction with water (Equation (1)) [51]. Furthermore, since the standard reduction potential of Fe^{3+}/Fe^{2+} (0.77 V) was higher than that of Mn^{4+}/Mn^{3+} (0.15 V), Fe^{3+} tended to be reduced to Fe^{2+} by Mn^{3+} (Equation (2)) [14]. The redox cycling of Fe^{3+}/Fe^{2+} and Mn^{4+}/Mn^{3+} regenerated Fe^{2+}, which also explained the increased content of Mn^{4+} after the reaction.

$$2Mn^{3+} + H_2O \rightarrow Mn^{4+} + Mn^{2+} + 4H^+ \quad (1)$$

$$Fe^{3+} + Mn^{3+} \rightarrow Fe^{2+} + Mn^{4+} \quad (2)$$

DFT calculations were conducted to elucidate the influence of SBC calcination temperature on the interfacial interaction and electron transfer behavior of $MnFe_2O_4$@SBC toward PI. As the calcination temperature increased from 350 to 750 °C, the I-O bonds in PI adsorbed on $MnFe_2O_4$@SBC were progressively elongated from 2.68 Å ($MnFe_2O_4$@SBC-350) to 3.87 Å ($MnFe_2O_4$@SBC-550) and further to 4.01 Å ($MnFe_2O_4$@SBC-750), indicating a continuous enhancement in PI activation (Figure 5a–c). Correspondingly, the calculated adsorption energies (E_{ads}) became more negative, increasing from −7.22 eV to −10.85 eV and reaching a maximum of −12.76 eV on $MnFe_2O_4$@SBC-750, suggesting the formation of a highly stable adsorption configuration. In contrast, further increasing the calcination temperature to 950 °C led to a decrease in both I-O bond elongation (3.82 Å) and E_{ads} (−8.71 eV), implying weakened interfacial interaction (Figure 5d). As shown in Figure 5e–h, the charge transfer values of $MnFe_2O_4$@SBC-350 (0.98 e) and $MnFe_2O_4$@SBC-550 (1.55 e) were significantly lower than that of $MnFe_2O_4$@SBC-750 (1.68 e), which can be attributed to excessive structural disorder at lower temperatures that limits π-electron delocalization and suppresses electron transport [52]. Meanwhile, $MnFe_2O_4$@SBC-950 exhibited a reduced Bader charge transfer (1.02 e) compared with $MnFe_2O_4$@SBC-750, indicating that excessive graphitization stabilizes π electrons and weakens interfacial electronic coupling with $MnFe_2O_4$. Notably, $MnFe_2O_4$@SBC-750 achieves an optimal balance between framework defects and graphitic domains. In this structure, defect-induced electron enrichment at interfacial sites enhances electronic polarization and reactivity, thereby facilitating efficient electron transfer from the catalyst to PI. This synergistic regulation of defect density and electronic structure explains the superior PI activation capability of $MnFe_2O_4$@SBC-750.

The electronic structures of $MnFe_2O_4$@SBC prepared at different calcination temperatures were further analyzed by total and projected density of states (TDOS and PDOS) calculations to elucidate the role of SBC structure in regulating interfacial electron transfer toward PI. As shown in Figure 5i,j, $MnFe_2O_4$@SBC-350 and $MnFe_2O_4$@SBC-550 exhibited a relatively low TDOS near the Fermi level, indicating limited availability of charge carriers on the surface of catalyst [53]. Although abundant structural defects were generated at low calcination temperature, excessive disorder broke the continuity of the π-conjugated framework. This led to strong localization of C 2p electrons and inhibited efficient electron transport (Figure 5m,n). Notably, $MnFe_2O_4$@SBC-750 exhibited the highest TDOS around the Fermi level, together with pronounced hybridization between C 2p and Mn/Fe 3d states (Figure 5k,o). This strong orbital overlap demonstrated the formation of π-d electronic coupling interface, which facilitated rapid electron delocalization across the carbon support and electron transfer from catalyst to the adsorbed PI [54]. In contrast, $MnFe_2O_4$@SBC-950

exhibited stabilized π electrons within the carbon framework due to excessive graphitization, weaking π-d electronic coupling with $MnFe_2O_4$ and suppressing electron transfer to the adsorbed PI (Figure 5l,p).

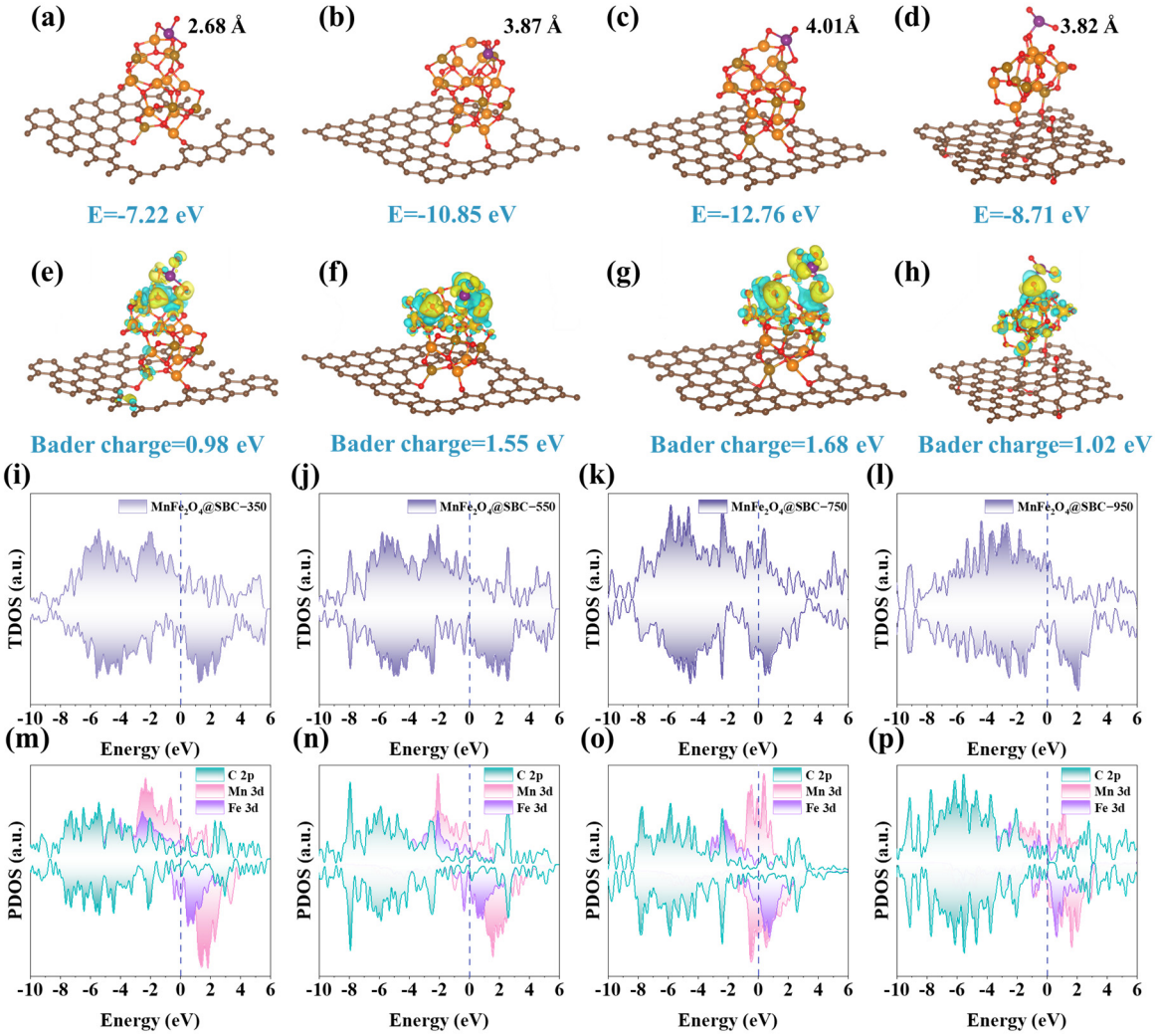

Figure 5. (**a**–**d**) Optimized adsorption geometries of IO_4^- on $MnFe_2O_4$@SBC-x with the corresponding E_{ads}, (**e**–**h**) charge density difference distributions of IO_4^- adsorbed on $MnFe_2O_4$@SBC_x, where yellow and cyan denote electron accumulation and depletion, (**i**–**l**) TDOS and (**m**–**p**) PDOS of $MnFe_2O_4$@SBC_x (E_f = 0 eV).

DFT calculations were further performed to examine the interaction mechanism of PI with SBC, $MnFe_2O_4$ and $MnFe_2O_4$@SBC. In the SBC/PI system, the four I-O bonds of PI remained relatively short (1.90 Å, 1.76 Å, 1.78 Å and 1.78 Å), indicating only weak perturbation of the oxidant structure. When PI was adsorbed on $MnFe_2O_4$, the I-O bonds were 2.77 Å, 2.34 Å, 2.28 Å and 2.16 Å, suggesting that $MnFe_2O_4$ possessed partial activation capability toward PI. Notably, in the $MnFe_2O_4$@SBC/PI system, the I-O bonds were markedly elongated to 3.87 Å, 1.92 Å, 1.91 Å and 1.90 Å, demonstrating that the I-O bonds become more susceptible to cleavage and subsequent activation of PI. The E_{ads} of PI on SBC, $MnFe_2O_4$ and $MnFe_2O_4$@SBC were calculated to be −0.79 eV, −4.53 eV and −10.85 eV, respectively. The significantly more favorable adsorption on $MnFe_2O_4$@SBC indicated the formation of a highly stable adsorption configuration, arising from enhanced electronic coupling between $MnFe_2O_4$ and SBC. Bader charge analysis further revealed that electron transfer from the catalysts to PI followed the order SBC (0.45 e) < $MnFe_2O_4$ (0.92 e) < $MnFe_2O_4$@SBC (1.58 e). The strong electron-donating properties of $MnFe_2O_4$@SBC

enhanced interfacial electronic polarization, thereby promoting the cleavage of the I-O bonds.

Overall, as illustrated in Figure 6, the PI activation performance of $MnFe_2O_4$@SBC originates from the synergistic regulation of defect structure, graphitization degree and interfacial electronic coupling. The optimized SBC framework constructed at appropriate calcination temperature provides abundant defect sites and a continuous π-conjugated network, which promotes π-electron delocalization and facilitates rapid interfacial electron transfer. Meanwhile, the strong π-d orbital coupling between C 2p and Mn/Fe 3d states enhances electronic polarization and accelerates electron migration from $MnFe_2O_4$@SBC to adsorbed PI, thereby weakening and elongating the I-O bonds of PI. In addition, the redox cycling of $Mn^{2+}/Mn^{3+}/Mn^{4+}$ and Fe^{2+}/Fe^{3+} further promotes ROS generation and sustains catalytic activity.

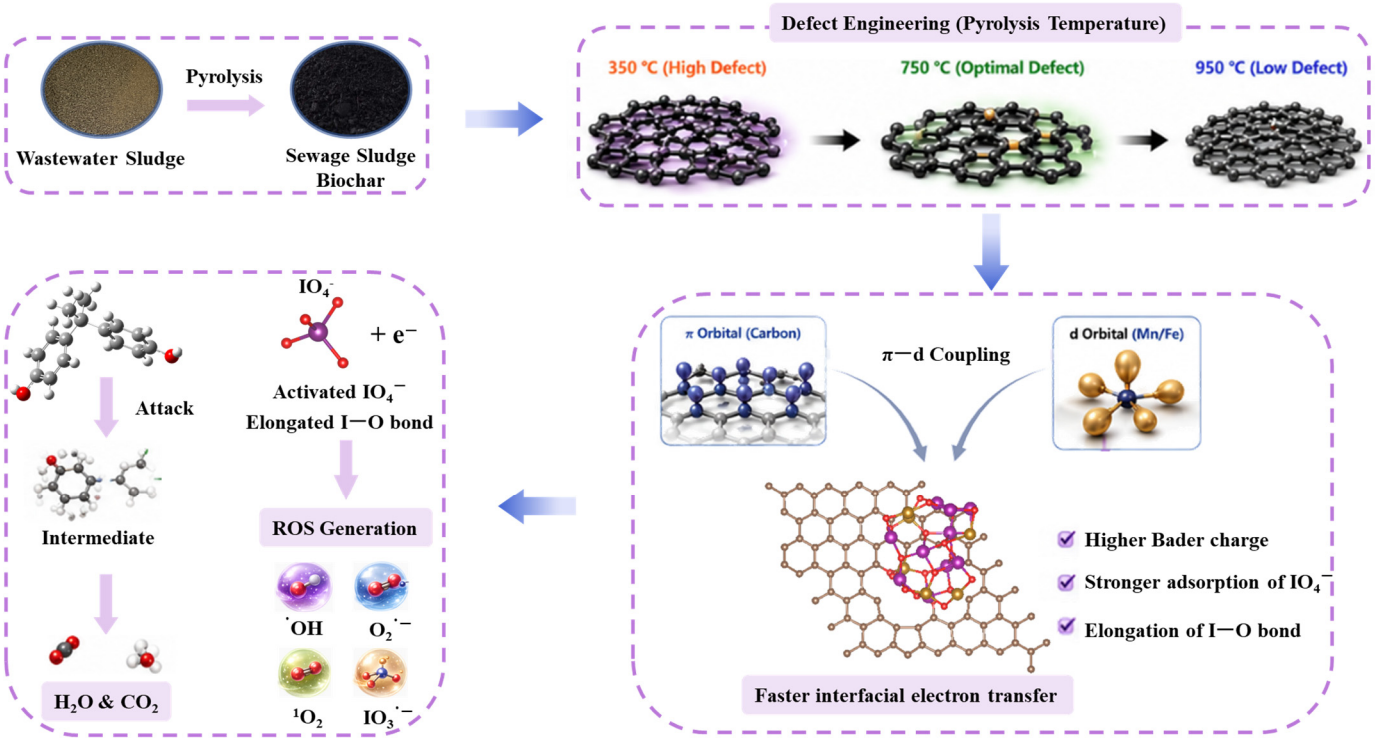

Figure 6. Mechanism of BPA degradation in $MnFe_2O_4$@SBC/PI.

3.5. Degradation Paths of BPA in the $MnFe_2O_4$@SBC/PI System

To further clarify the reactive regions of BPA in the $MnFe_2O_4$@SBC/PI system, frontier molecular orbital analysis was performed using DFT calculations. As shown in Figure 7a, the highest occupied molecular orbitals (HOMO) were predominantly localized on the aromatic rings and the phenolic oxygen atoms, indicating that these electron-rich domains served as the primary electron-donating sites during oxidative reactions [55]. In contrast, the lowest unoccupied molecular orbitals (LUMO) were mainly distributed over several carbon atoms on the benzene rings, suggesting that these positions function as favorable electron-accepting sites [56]. The calculated HOMO (−6.024 eV) and LUMO (−0.213 eV) levels resulted in an energy gap of 5.811 eV, reflecting a relatively stable molecular structure. However, such a gap still permits electrophilic, nucleophilic and radical attacks when strong oxidizing species ($^{\bullet}OH$, $O_2^{\bullet-}$, $IO_3^{\bullet}$ and $^1O_2$) were present in the $MnFe_2O_4$@SBC/PI system. The electrostatic potential (ESP) surface further showed strong negative potential around the phenolic oxygens and nearby ortho-carbons, indicating that these electron-rich sites were susceptible to electrophilic oxidation (Figure 7b). The relatively neutral to slightly

positive regions located on the isopropylidene bridge and para-positions of the aromatic rings provide additional pathways for nucleophilic or radical attacks [57].

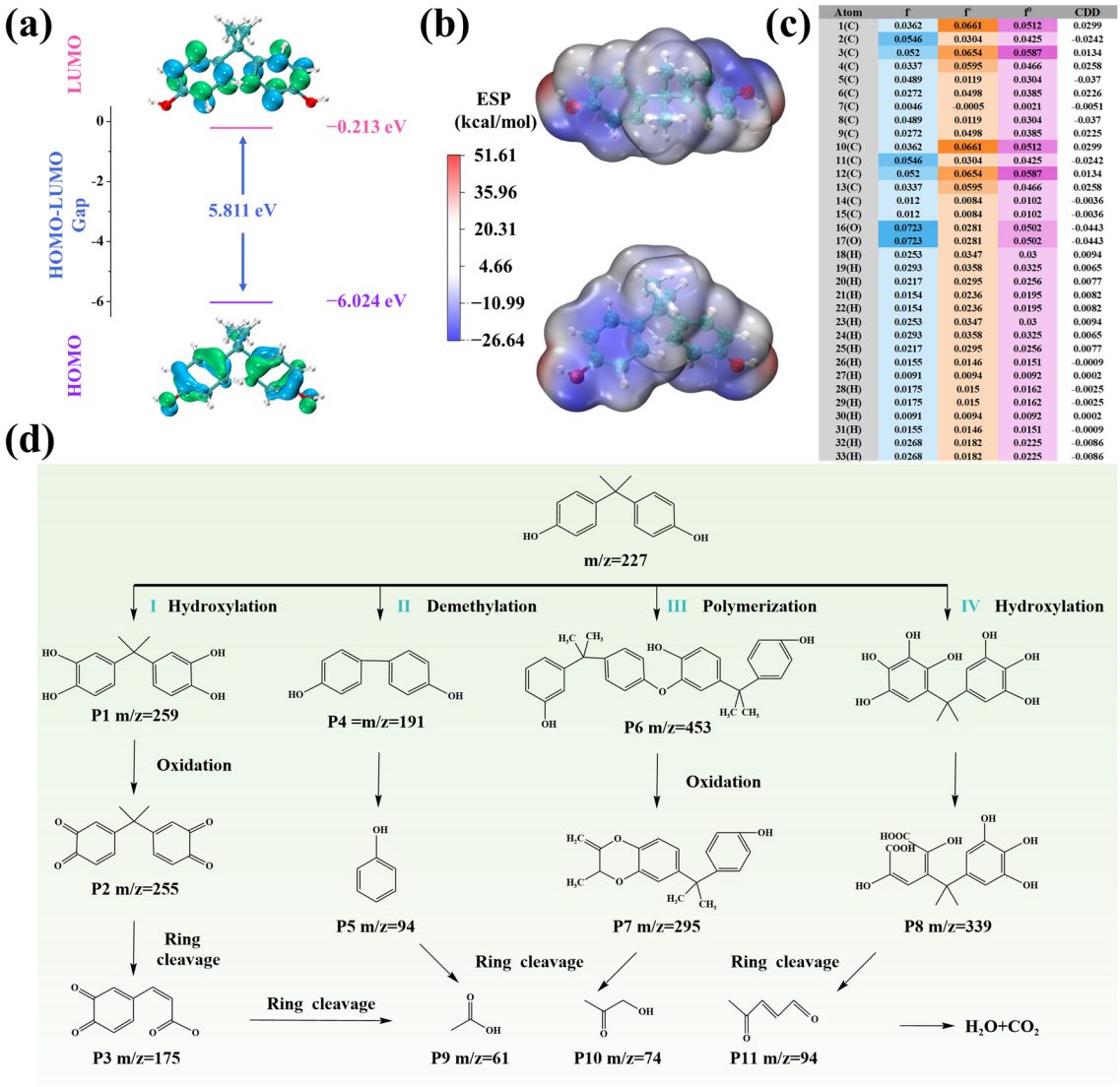

Atom	f⁻	f⁺	f⁰	CDD
1(C)	0.0362	0.0661	0.0512	0.0299
2(C)	0.0546	0.0304	0.0425	-0.0242
3(C)	0.052	0.0654	0.0587	0.0134
4(C)	0.0337	0.0595	0.0466	0.0258
5(C)	0.0489	0.0119	0.0304	-0.037
6(C)	0.0272	0.0498	0.0385	0.0226
7(C)	0.0046	-0.0005	0.0021	-0.0051
8(C)	0.0489	0.0119	0.0304	-0.037
9(C)	0.0272	0.0498	0.0385	0.0225
10(C)	0.0362	0.0661	0.0512	0.0299
11(C)	0.0546	0.0304	0.0425	-0.0242
12(C)	0.052	0.0654	0.0587	0.0134
13(C)	0.0337	0.0595	0.0466	0.0258
14(C)	0.012	0.0084	0.0102	-0.0036
15(C)	0.012	0.0084	0.0102	-0.0036
16(O)	0.0723	0.0281	0.0502	-0.0443
17(O)	0.0723	0.0281	0.0502	-0.0443
18(H)	0.0253	0.0347	0.03	0.0094
19(H)	0.0293	0.0358	0.0325	0.0065
20(H)	0.0217	0.0295	0.0256	0.0077
21(H)	0.0154	0.0236	0.0195	0.0082
22(H)	0.0154	0.0236	0.0195	0.0082
23(H)	0.0253	0.0347	0.03	0.0094
24(H)	0.0293	0.0358	0.0325	0.0065
25(H)	0.0217	0.0295	0.0256	0.0077
26(H)	0.0155	0.0146	0.0151	-0.0009
27(H)	0.0091	0.0094	0.0092	0.0002
28(H)	0.0175	0.015	0.0162	-0.0025
29(H)	0.0175	0.015	0.0162	-0.0025
30(H)	0.0091	0.0094	0.0092	0.0002
31(H)	0.0155	0.0146	0.0151	-0.0009
32(H)	0.0268	0.0182	0.0225	-0.0086
33(H)	0.0268	0.0182	0.0225	-0.0086

Figure 7. (**a**) LUMO and HOMO distribution of BPA and HOMO-LUMO gap, (**b**) top view and front view of the ESP mapping of BPA, (**c**) fukui index f^-, f^+ and f^0 of BPA and (**d**) degradation pathways.

In addition, the condensed Fukui functions were calculated to identify atom-specific reactivity toward electrophilic (f^-), radical (f^0), and nucleophilic (f^+) species (Figures 7c and S9). Atoms O16, O17, C2, C3, C11 and C12 exhibited relatively high f^- values, suggesting that these positions were particularly vulnerable to electrophilic oxidants [58]. Meanwhile, atoms C1, C3, C10, C12, O16 and O17 showed elevated f^0 values, indicating their pronounced reactivity toward radical species such as $^{\bullet}OH$ and $IO_3^{\bullet}$ [59]. Furthermore, the f^+ values were higher at C1, C10, C3, C12, C4 and C13, indicating that these positions are more susceptible to nucleophilic radical attack by $O_2^{\bullet-}$ [60]. The condensed dual descriptor (CDD) analysis revealed large absolute values around the phenolic hydroxyl groups and aromatic carbons (O16, O17, C5, C8, C1 and C10), confirming that these regions are the dominant reactive centers during BPA transformation [61]. These results demonstrated that the oxidative degradation of BPA over $MnFe_2O_4$@SBC was strongly governed by electrophilic and radical attack at electron-rich oxygen and carbon sites, consistent with the experimentally observed degradation behavior.

To elucidate intermediate products of BPA in the $MnFe_2O_4$@SBC/PI system, the intermediates detected by LC-MS were used to propose four possible degradation pathways, as shown in Figures 7d and S10. In Pathway I, $^{\bullet}OH$ and $IO_3^{\bullet}$ preferentially targeted the electron-rich carbon sites adjacent to the phenolic hydroxyl groups of BPA molecule (C1, C3, C10, C12), producing the hydroxylated intermediate P1 (m/z = 259). Subsequent multi-step oxidation of P1 yielded the quinone-type species P2 (m/z = 255), which then underwent oxidative ring-opening to generate P3 (m/z = 175) [62]. Pathway II involved $^1O_2$ mediated oxidative demethylation of BPA, forming P4 (m/z = 191). Further oxidation of P4 led to cleavage of the isopropylidene bridge, producing low-molecular-weight phenolic fragments P5 (m/z = 94) [63]. In Pathway III, BPA underwent radical-induced polymerization followed by oxidative coupling, generating a dimeric intermediate P6 (m/z = 453). Progressive oxidation of this dimer produced P7 (m/z = 295), indicating that polymerization–depolymerization cycles contributed to BPA degradation [64]. Pathway IV proceeded through direct hydroxylation and aromatic ring scission to generate P8 (m/z = 339) [65]. Ultimately, P3, P5, P7 and P8 were further attacked by ROS to undergo ring-opening and fragmentation reactions, producing small organic acids and low-molecular-weight compounds P9 (m/z = 61), P10 (m/z = 74) and P11 (m/z = 94) [66,67]. These species were subsequently mineralized to CO_2 and H_2O.

3.6. Stability and Practical Applicability of $MnFe_2O_4$@SBC

The durability and practical applicability of the $MnFe_2O_4$@SBC/PI system were systematically evaluated through cyclic experiments, mineralization analysis, and degradation tests of multiple pollutants. As shown in Figure S11, the catalytic performance gradually declined with repeated use, with BPA removal efficiencies decreasing from 98.6% in the first cycle to 86.3%, 80.7%, 75.0% and 64.3% in subsequent cycles. This attenuation can be primarily attributed to the partial blockage of active sites by accumulated intermediates and the consumption of surface reactive centers during continuous PI activation. In addition, the $MnFe_2O_4$@SBC/PI system achieved a TOC removal efficiency of 69.2%, indicating its capability for mineralization of BPA (Figure S12).

To further assess the universality of this system, a range of organic contaminants were selected, including BPA, sulfamethoxazole (SCP), acetaminophen (ACE), and ciprofloxacin (CIP). The removal efficiencies were 98.6% (BPA), 98.2% (SCP), 95.9% (ACE), and 81.7% (CIP), respectively (Figure S13). The relatively lower degradation efficiency of CIP can be attributed to its more stable molecular structure and higher ionization potential, which makes electron abstraction and oxidative transformation less favorable compared with other pollutants. These results confirm that the $MnFe_2O_4$@SBC/PI system exhibits broad-spectrum applicability toward diverse organic contaminants.

Moreover, the formation of toxicity of degradation products, iodine-containing by-products and the influence of coexisting inorganic anions were carefully examined and are presented in Text S9–S11. The results demonstrated that PI was predominantly converted into environmentally benign IO_3^- without generating toxic iodinated species. The presence of common anions exerted negligible effects on BPA degradation efficiency, indicating the environmental safety and robustness of the system.

4. Conclusions

In this study, a series of defect-engineered $MnFe_2O_4$@SBC catalysts were successfully synthesized by coupling spinel $MnFe_2O_4$ with sewage sludge-derived biochar prepared at different calcination temperatures. Among them, $MnFe_2O_4$@SBC-750 exhibited the best catalytic performance, achieving 98.6% BPA removal within 30 min during PI activation. Structural characterization revealed that the superior activity of $MnFe_2O_4$@SBC-750 origi-

nated from its optimized carbon framework containing an appropriate balance between defect density and graphitization degree. This structural feature promoted interfacial electronic interaction between $MnFe_2O_4$ and SBC, thereby facilitating PI adsorption, electron transfer, and I-O bond activation. Mechanistic investigations demonstrated that $^{\bullet}OH$, $O_2^{\bullet-}$, $IO_3^{\bullet}$ and $^1O_2$ jointly contributed to BPA degradation, while electrochemical analysis and DFT calculations further confirmed that defect-regulated π-d electronic coupling accelerated interfacial charge transfer and enhanced PI activation efficiency. Importantly, this work demonstrates that catalytic activity is not governed solely by defect abundance, but rather by the synergistic balance between structural defects and electronic delocalization. Overall, this study provides new insight into the role of defect regulation in spinel-carbon catalysts and offers a promising strategy for designing efficient biochar-based catalysts for advanced oxidation processes and environmental remediation.

Supplementary Materials: The following supporting information can be downloaded at: https://www.mdpi.com/article/10.3390/w18111262/s1, Figure S1: SEM images and EDS mappings of (a) $MnFe_2O_4$, (b) SBC and (c) $MnFe_2O_4$@SBC; Figure S2: N_2 adsorption-desorption isotherms (BET analysis) and corresponding pore size distribution curves (BJH method) of (a) SBC, (b) $MnFe_2O_4$ and (c) $MnFe_2O_4$@SBC; Figure S3: Pseudo-first-order rate constants for BPA degradation under different conditions, including (a) $MnFe_2O_4$@SBC synthesized with different $MnFe_2O_4$: SBC ratios, (b) $MnFe_2O_4$@SBC catalysts prepared from SBC calcined at different temperatures and (c) different systems; Figure S4: Pseudo-first-order rate constants for BPA degradation in the presence of different quenchers, including (a) MeOH, (b) p-BQ, (c) FFA, (d) phenol, (e) DMSO and (f) $K_2Cr_2O_7$; Figure S5: PI consumption in the presence of FFA; Figure S6: 2,4,6-TCP degradation efficiency in the $MnFe_2O_4$@SBC/PI system (reaction conditions: [$MnFe_2O_4$@SBC] = 0.4 g L^{-1}, [2,4,6-TCP] = 20 mg L^{-1}, [PI] = 0.5 mM, initial pH = 7; Figure S7: BPA removal efficiency under different pre-mixing times in the $MnFe_2O_4$@SBC/PI system; Figure S8: High-resolution XPS spectra of $MnFe_2O_4$@SBC before and after reaction: (a) C 1s, (b) O 1s, (c) Mn 2p and (d) Fe 2p spectra; Figure S9: Detailed symbol and atomic number of the BPA molecule; Figure S10: LC-MS spectra of intermediate products formed during BPA degradation in the $MnFe_2O_4$@SBC/PI system at different reaction times; Figure S11: Reusability of $MnFe_2O_4$@SBC for BPA degradation in five cycles; Figure S12: TOC removal efficiency of BPA in the $MnFe_2O_4$@SBC/PI system; Figure S13: Degradation performance of various organic pollutants in the $MnFe_2O_4$@SBC/PI system; Figure S14: (a) Full scan spectrum of SBC, high-resolution XPS spectra of (b) C1s, (c) O1s (d) Mn2p and (e) Fe2p of SBC; Figure S15: Effect of (a) catalyst dosage, (b) BPA concentration, (c) PI concentration and (d) initial pH on BPA degradation (reaction conditions: [$MnFe_2O_4$@SBC] = 0.4 g L^{-1}, [BPA] = 20 mg L^{-1}, [PI] = 0.5 mM and initial pH = 7); Figure S16: Pseudo-first-order rate constants for BPA degradation under different conditions, including (a) catalyst dosage, (b) BPA concentration, (c) PI concentration and (d) initial pH (reaction conditions: [$MnFe_2O_4$@SBC] = 0.4 g L^{-1}, [BPA] = 20 mg L^{-1}, [PI] = 0.5 mM and initial pH = 7); Figure S17: (a) I-t curves and (b) LSC on $MnFe_2O_4$@SBC electrodes; Figure S18: T.E.S.T toxicity analysis of various intermediates: (a) oral LD50 in rats, (b) bioaccumulation factor, (c) developmental toxicity and (d) mutagenic developmental toxicity; Figure S19: (a) Changes in iodine species concentrations during the $MnFe_2O_4$@SBC/PI reaction, (b) BPA removal performance in the $MnFe_2O_4$@SBC/$NaIO_3$ and $MnFe_2O_4$@SBC/KI systems, (c) HOI formation in the $MnFe_2O_4$@SBC/PI system, (d) Identification of I_2 and I_3^- species in the $MnFe_2O_4$@SBC/PI system; Figure S20: Influence of different inorganic anions and HA on BPA degradation in the $MnFe_2O_4$@SBC/PI system: (a) Cl^-, (b) SO_4^{2-}, (c) HCO_3^-, (d) CO_3^{2-}, (e) HPO_4^{2-} and (f) HA (reaction conditions: [$MnFe_2O_4$@SBC] = 0.4 g L^{-1}, [BPA] = 20 mg L^{-1}, [PI] = 0.5 mM and initial pH = 7); Figure S21: Kinetics of BPA degradation in the presence of various inorganic anions and HA in the $MnFe_2O_4$@SBC/PI system: (a) Cl^-, (b) SO_4^{2-}, (c) HCO_3^-, (d) CO_3^{2-}, (e) HPO_4^{2-} and (f) HA (reaction conditions: [$MnFe_2O_4$@SBC] = 0.4 g L^{-1}, [BPA] = 20 mg L^{-1}, [PI] = 0.5 mM and initial pH = 7); Table S1: HPLC methods for the determination of organic pollutants and iodine species; Table S2: Specific surface area and average pore volume of $MnFe_2O_4$@SBC; Table S3: The comparison

of efficiency towards pollutants degradation in different systems. References [68–78] are cited in the Supplementary Materials.

Author Contributions: B.Y.: Conceptualization, Methodology, Data curation, Formal analysis, Conceptualization. H.Z.: Investigation, Conceptualization, Methodology, Data curation, Formal analysis, Conceptualization, Writing—original draft. H.L. (Hao Lu): Methodology. H.L. (Haibo Li): Investigation, Conceptualization. B.L.: Writing—review and editing, Funding acquisition, Project administration. All authors have read and agreed to the published version of the manuscript.

Funding: This work was supported by Study on the Tianjin Natural Science Foundation (No. 25JCYBJC00200) and Ecological Compensation Mechanism and Biological Invasion Risk of the Western Route of the South-to-North Water Diversion Project (No. 2022YFC32002204).

Data Availability Statement: The original contributions presented in this study are included in the article/Supplementary Materials. Further inquiries can be directed to the corresponding author.

Acknowledgments: During the preparation of this manuscript, the authors used ChatGPT 5.0 for the purposes of drawing and designing the graphical abstract. The authors have reviewed and edited the output and take fully responsible for the content of this publication.

Conflicts of Interest: The authors declare no conflict of interest.

References

1. Hu, P.; Qian, Y.; Radian, A.; Xu, M.; Guo, C.; Gu, J.-D. A global metagenomics-based analysis of BPA degradation and its coupling with nitrogen, sulfur, and methane metabolism in landfill leachates. *J. Hazard. Mater.* **2024**, *477*, 135395. [CrossRef]
2. Cerrón-Calle, G.A.; Flores, M.; Roldan, M.A.; Flores, K.; Brillas, E.; dos Santos, A.J.; Garcia-Segura, S. Electrochemical persulfate activation for degradation of BPA using a novel self-standing CuO_x/CoO_x cathode. *Chem. Eng. J.* **2025**, *519*, 164960. [CrossRef]
3. Liu, J.; Liang, S.; Xiang, T.; Li, L.; Gao, P.; Zhou, J. S-vacancy-rich MoS_2 for enhanced BPA degradation involved peroxymonosulfate activation: Sustainable transformation of toxic V(V) into a homogeneous catalyic system. *J. Water Process Eng.* **2025**, *77*, 108542. [CrossRef]
4. Wang, P.; Zhang, Y.; Zhu, J.; Wei, J.; Qi, J.; Cao, T.; Yang, M. Catalytic degradation of BPA by bamboo leaf-derived KOH-activated porous biocarbon loaded with $CoFe_2O_4$-activated peroxymonosulfate. *Chem. Eng. J.* **2024**, *492*, 151886. [CrossRef]
5. Ouyang, S.; Zhao, H.-P.; Lai, C.-Y. Propane-driven efficient BPA degradation in groundwater: Transformation pathways, microbial ecology and enzymatic mechanisms in a membrane biofilm reactor. *J. Hazard. Mater.* **2025**, *499*, 140214. [CrossRef]
6. Mojiri, A.; Zhou, J.L.; Farahani, S. Advancements in photocatalysis and machine learning for bisphenol A (BPA) degradation in aquatic systems: A critical review. *J. Clean. Prod.* **2025**, *518*, 145919. [CrossRef]
7. Shah, N.A.; Chen, X.; Javed, A.; Qu, J.; Zhang, Y. A comparative study on degradation kinetics and toxicity changes of BPA and BPS in UV-based advanced oxidation processes. *Environ. Res.* **2025**, *284*, 122223. [CrossRef]
8. Shen, Y.; Huang, J.; Qiao, J.; Chen, J.; Batjargal, E.; Tuulaikhuu, B.-A.; Qian, Y.; Zhou, X.; Zhang, Y. Metal-based activation of periodate as an advanced oxidation process for water decontamination: A critical review. *Chem. Eng. J.* **2025**, *513*, 162949. [CrossRef]
9. Wu, Y.; Yang, G.; Wang, L.; Long, J.; Zhu, M.; Zhang, S.; Han, J.; Han, C.; Wang, G.; Wu, X.; et al. Crystalline phase engineering of bismuth molybdates unlocks efficient periodate activation for visible-light driven contaminant degradation. *Appl. Catal. B Environ. Energy* **2026**, *383*, 126144. [CrossRef]
10. Li, S.; Zhang, X.; Zheng, H.; Leong, Y.K.; Li, T.; Luo, Z.; Chang, J.-S. Black phosphorus quantum dots modulate the electronic structure of $Bi_{12}MnO_{20}$ catalyst to enhance periodate activation and $^1O_2$-dominated tetracycline hydrochloride degradation under microwave irradiation. *Appl. Catal. B Environ. Energy* **2026**, *385*, 126324. [CrossRef]
11. Liu, Y.; Li, R.; Wen, L.; Li, S.; Liu, M.; Li, X.; Huang, Z.; Ding, D.; Yang, S.; Chen, Y.; et al. Dynamic inner-outer dual-cycles drive selective periodate activation for nearly exclusive singlet oxygen production toward sustainable water purification. *Water Res.* **2026**, *292*, 125400. [CrossRef]
12. Chen, X.; Zhuo, Y.; Huang, X.; Qin, T.; Peng, H.; Yang, J.; Zhou, Y. Applications of periodate activation for emerging contaminants treatment in water: Activation methods, reaction parameters and mechanism. *Environ. Res.* **2025**, *271*, 121088. [CrossRef] [PubMed]
13. Li, S.; Liu, Y.; Zheng, H.; Leong, Y.K.; Huangfu, X.; Gierczak, T.; Witkowski, B.; Chang, J.-S. Crucial role of Mn-doped FeNi layered double hydroxide in periodate activation toward enhancement of Fe(IV) and carbonate radical (·CO− 3) production. *Chem. Eng. J.* **2025**, *520*, 166380. [CrossRef]

14. Xu, W.; Zheng, X.; Shangguan, Z.; Qu, J.; Zhang, W. A low-cost magnetic catalyst ($MnFe_2O_4$) for ciprofloxacin degradation via periodate activation: The synergistic effect of Mn and Fe. *Chem. Eng. J.* **2023**, *464*, 142562. [CrossRef]
15. Gong, Z.; Zhu, H.; Huang, M.; Oh, W.; Wu, X.; Zhou, T. An unveiled trade-off of biochar properties for selective oxidation of wastewater beyond Fenton-conditioned dewatering of sewage sludge. *Water Res.* **2026**, *292*, 125317. [CrossRef]
16. Zhu, Y.; Liu, S.; Wang, C.; Yu, P.; Chen, C. Unlocking the hidden power: Magnetic sludge biochar as a strengthening agent for anammox nitrogen removal advancement and microbial metabolic cooperation. *Chem. Eng. J.* **2026**, *527*, 171954. [CrossRef]
17. Ma, K.; Lu, Y.; Yang, Y.; Cui, Y.; Yu, X.; Xu, J.; Zhao, K.; Bai, C.; Wakisaka, M. Synergistic activation of persulfate by crab Shell-sludge derived biochar for enhanced Ofloxacin degradation: Mechanistic insights and performance evaluation. *Sep. Purif. Technol.* **2026**, *387*, 136711. [CrossRef]
18. He, L.; Yang, S.; Yang, L.; Shen, S.; Li, Y.; Kong, D.; Chen, Z.; Yang, S.; Wang, J.; Wu, L.; et al. Ball milling-assisted preparation of sludge biochar as a novel periodate activator for nonradical degradation of sulfamethoxazole: Insight into the mechanism of enhanced electron transfer. *Environ. Pollut.* **2023**, *316*, 120620. [CrossRef]
19. He, L.; Yang, S.; Shen, S.; Ma, Y.; Chen, Y.; Xue, J.; Wang, J.; Zheng, L.; Wu, L.; Zhang, Z.; et al. Novel insights into the mechanism of periodate activation by heterogeneous ultrasonic-enhanced sludge biochar: Relevance for efficient degradation of levofloxacin. *J. Hazard. Mater.* **2022**, *434*, 128860. [CrossRef]
20. Yu, Y.; Li, Y.; Liu, Y.; Chen, Z.; Wu, L.; Yang, L. Electron-transfer driven efficient degradation of sulfamethoxazole by Fe-Mg bimetallic modified sewage sludge biochar activated periodate. *Process Saf. Environ. Prot.* **2025**, *199*, 107130. [CrossRef]
21. Li, X.; Zhao, Y.; Yuan, T.; Zhang, Y.; Shu, X.; Lu, X. Periodate activation by $MnFe_2O_4$ spinel for sulfamethoxazole degradation: Iodate radical dominance, degradation pathway, DFT calculation and toxicity assessment. *Sep. Purif. Technol.* **2024**, *347*, 127553. [CrossRef]
22. Huang, J.; Tong, H.; Shi, D.; Xu, S.; Wen, X.; Fu, K.; Xie, H.; Cai, H.; Liu, J.; Tang, S.; et al. Efficient activation of periodate using $MnFe_2O_4$/BC composite for removal of organic contaminants: Performance and mechanism. *Sep. Purif. Technol.* **2024**, *345*, 127404. [CrossRef]
23. Ji, S.; Wang, Y.; Liu, H.; Lu, X.; Guo, C.; Xin, S.; Horton, J.H.; Zhan, F.; Wang, Y.; Li, Z. Regulating the Electronic Synergy of Asymmetric Atomic Fe Sites with Adjacent Defects for Boosting Activity and Durability toward Oxygen Reduction. *Adv. Funct. Mater.* **2024**, *34*, 2314621. [CrossRef]
24. Luo, X.; Wei, W.; Xu, Y.; Liu, D.; Wei, Z.; Liu, J.; Li, Z.; Wang, L.; Ouyang, S.; Yuan, H.; et al. Neighboring Carbon Defects Enhanced Molecular Oxygen Activation of Cobalt Single Atom Catalysts Toward Efficient Aerobic Alcohols Oxidation. *Angew. Chem.* **2025**, *137*, e202502430. [CrossRef]
25. Wang, C.; Hu, Z.; Wang, Z.; Zhao, H.; He, M.; Li, D.; Zhou, W. Synergistic modulation of in-plane N-doping and intrinsic vacancy defects in activated carbon for enhanced formaldehyde adsorption. *Environ. Res.* **2026**, *290*, 123492. [CrossRef]
26. Sun, X.; Wu, K.; Yang, G.; Shen, F.; Zhang, S.; Wu, T.; Sun, S.; Jiang, Y.; Wu, X. Synergistic effect of carbon defects and iron active sites in biochar-activated peroxymonosulfate for acetaminophen degradation: Unlocking the non-radical mechanisms. *Chem. Eng. J.* **2025**, *523*, 168775. [CrossRef]
27. Zhang, X.; Li, C.; Chen, T.; Tan, Y.; Liu, X.; Yuan, F.; Zheng, S.; Sun, Z. Enhanced visible-light-assisted peroxymonosulfate activation over $MnFe_2O_4$ modified g-C3N4/diatomite composite for bisphenol A degradation. *Int. J. Min. Sci. Technol.* **2021**, *31*, 1169–1179. [CrossRef]
28. Yu, Y.; Chen, X.; Tao, L.; Li, Y.; Wu, L.; Chen, Z.; He, X.; Luo, Y.; Yang, L. Fe-Mn bimetallic loaded sludge biochar as a novel periodate activator for sulfamethoxazole removal: The combination of radical and non-radical mechanisms. *Environ. Res.* **2025**, *285*, 122515. [CrossRef]
29. Zang, H.; Huang, Y.; Hao, T.; Xiao, S.; Zhang, J.; Li, H.; Yan, B. Fe–Modified and N–Doped sludge biochar for BPA Removal: PI-Activated Nonradical oxidation Coupled with synergistic adsorption. *Sep. Purif. Technol.* **2025**, *379*, 135124. [CrossRef]
30. Li, S.; Li, J.; Shi, D.; Sofer, Z.; Zhou, H. Magnetically driven BiOI/$MnFe_2O_4$ micro/nanorobots for capture, aggregation, and on-site decontamination of biological warfare agents. *Sep. Purif. Technol.* **2026**, *380*, 135351. [CrossRef]
31. Pan, Y.; Li, N.; Wu, C.; Zhou, Q.; Li, K.; Li, S. Superior room-temperature efficacy of selective catalytic reduction of NOx by CO utilizing metal-modified Fe_2O_3 catalysts. *Chem. Eng. J.* **2024**, *487*, 150698. [CrossRef]
32. Shao, S.; Wang, J.; Li, P.; Zhou, R.; Zhang, M. Enhanced tetracycline elimination through periodate activation via biochar-loaded crystallographic manganese dioxide –Electron transfer mechanism facilitated by oxygen vacancies. *Sep. Purif. Technol.* **2025**, *378*, 134788. [CrossRef]
33. Zhang, X.; Liyakat, A.; Kamali, M.; Li, J.; Van der Bruggen, B.; Huang, C.-H.; Cabooter, D.; Dewil, R. Electron transfer centers facilitate the degradation of antibiotics with an O-doped walnut shell biochar/periodate system. *Chem. Eng. J.* **2025**, *520*, 166227. [CrossRef]
34. Qin, L.; Hu, S.; Yi, H.; Wang, W.; Lai, C.; Liu, S.; Ma, D.; Tong, T.; Deng, H.; Lv, G. B-doped lotus pollen biochar photothermal activating periodate for acetaminophen degradation by non-radical pathway: Significance of thermal effect from the photothermal process. *Sep. Purif. Technol.* **2025**, *375*, 133707. [CrossRef]

35. Lin, X.; Ge, Q.; Zhou, X.; Wang, Y.; Zhu, C.; Liu, K.; Wan, J. Nitrogen doping enhances PMS activation by $MnFe_2O_4$-NBC through generating active sites and establishing an internal electric field. *J. Water Process Eng.* **2025**, *77*, 108359. [CrossRef]
36. Elmitwalli, T.; Fouad, M.; Mossad, M.; Samy, M. Periodate activation by mulukhiyah stalks and potato peels-derived biochars for the efficient degradation of sulfamethazine. *J. Environ. Chem. Eng.* **2024**, *12*, 112101. [CrossRef]
37. Seo, G.; Narendra Kumar, A.V.; Shin, W.S. Periodate activation and pH regulation using ball-milled metal-oxide-mineral-biochar composite for removal of antibiotics from contaminated water. *Environ. Res.* **2024**, *260*, 119611. [CrossRef]
38. Song, Z.; Shi, Y.; Zhang, H.; Zhang, B.; Zhou, H.; Xia, D. DMF etching-free pore-making synergy: Alkaline lignin-derived biochar for non-radical PMS activation toward efficient BPA degradation. *Environ. Res.* **2025**, *286*, 123026. [CrossRef]
39. Ji, X.; Lin, H.; Zhang, Y.; Lu, J.; Zhang, Y.; Sun, H.; Wang, G.; Yang, X.; Li, W.; Duan, J.; et al. Activation of peroxymonosulfate by magnesium−modified biochar for the degradation of imidacloprid: Effectiveness and mechanisms. *Chem. Eng. J.* **2025**, *524*, 169498. [CrossRef]
40. Wang, Y.; Jiao, H.; Liu, Z.; Yang, S.; Chen, R.; Liu, C.; Dai, J.; Ding, D. Biochar alters the selectivity of $MnFe_2O_4$-activated periodate process through serving as the electron-transfer mediator. *J. Hazard. Mater.* **2024**, *472*, 134530. [CrossRef]
41. Wang, W.; Shi, Q.; Wu, T.; Zheng, S.; Xu, Z.; Zhu, W. Fe/S co-doped biochar catalysts for enhanced peroxymonosulfate activation: Synergistic effects of catalysis and anti-deactivation on antibiotic degradation. *J. Clean. Prod.* **2025**, *533*, 147005. [CrossRef]
42. Lu, J.; Deng, X.; Huang, X.; Chen, C.; Liang, J.; Tong, Z. N-doping biochar-supported Fe-Cu bimetallic catalyst for H_2O_2 activation to remove tetracycline: Mechanism insight and performance optimization. *J. Environ. Manag.* **2025**, *395*, 127804. [CrossRef]
43. Xing, J.; Zhou, S.; Ge, M.; Sun, Z.; Cai, S.; Li, Y.; Xu, M. Interfacial electron transfer facilitated the bioreduction of biochar-sorbed organic pollutants: Division-of-labor roles of electroactive structures. *Water Res.* **2026**, *291*, 125170. [CrossRef] [PubMed]
44. Pan, X.; Ma, H.; Zhang, R.; Deng, R.; Li, M.; Yang, B.; Zhu, R.; Zhao, L.; Liu, Y.; Gong, X. Manganese on P, N self-doped biochar toward promoting periodate activation for highly efficient tetracycline degradation: Performance and mechanisms. *J. Environ. Chem. Eng.* **2025**, *13*, 115809. [CrossRef]
45. Chen, L.; Yang, Y.; Tang, W.; Huang, H. Pyrolysis of nitrilotriacetic acid-Mn/Fe to produce $MnFe_2O_4$/C nanoparticles: Excellent performance of activating periodate to degrade organic pollutants. *Process Saf. Environ. Prot.* **2025**, *193*, 239–250. [CrossRef]
46. Guo, Y.; Long, J.; Huang, J.; Yu, G.; Wang, Y. Can the commonly used quenching method really evaluate the role of reactive oxygen species in pollutant abatement during catalytic ozonation? *Water Res.* **2022**, *215*, 118275. [CrossRef]
47. Zhang, M.; Lin, T.; Chen, H. Exploration of low-dose ozone-activated periodate (O_3/IO_4^-) for rapid degradation of the β-Blocker pindolol: Efficiency and radical mechanism. *Water Res.* **2025**, *285*, 124116. [CrossRef]
48. Luo, K.; Shi, Y.; Huang, R.; Wei, X.; Wu, Z.; Zhou, P.; Zhang, H.; Wang, Y.; Xiong, Z.; Lai, B. Activation of periodate by N-doped iron-based porous carbon for degradation of sulfisoxazole: Significance of catalyst-mediated electron transfer mechanism. *J. Hazard. Mater.* **2023**, *457*, 131790. [CrossRef]
49. Feng, H.; Yin, P.; Yang, L.; Liu, L.; Cai, Y.; Fang, J.; Yang, Y. Tailoring Fe 3d spin states for enhanced adsorption/activation of in situ generated H_2O_2 on S-doped magnetite@resorcinol-formaldehyde resins core-shell catalysts toward boosted cascade self-Fenton oxidation. *Chem. Eng. J.* **2025**, *522*, 167917. [CrossRef]
50. Han, H.; Chen, M.; Sun, C.; Han, Y.; Xu, L.; Zhao, Y. Synergistic enhancement in hydrodynamic cavitation combined with peroxymonosulfate fenton-like process for bpa degradation: New insights into the role of cavitation bubbles in regulation reaction pathway. *Water Res.* **2025**, *268*, 122666. [CrossRef]
51. Fang, G.; Li, J.; Zhang, C.; Qin, F.; Luo, H.; Huang, C.; Qin, D.; Ouyang, Z. Periodate activated by manganese oxide/biochar composites for antibiotic degradation in aqueous system: Combined effects of active manganese species and biochar. *Environ. Pollut.* **2022**, *300*, 118939. [CrossRef]
52. Zhang, Y.; Xuan, K.; Zhu, Z.; Zhong, L.; Othman, R.M.; Lithoxoos, G.P.; Shakhs, A.N.; Almansour, F.; Zeng, X.; Sun, X.; et al. Quantifying the co-evolution of micro- and meso-structure defects and their influence on CO_2 capture capacity of KOH-activated zeolite-templated carbon in dry and humid conditions. *Sep. Purif. Technol.* **2026**, *382*, 136082. [CrossRef]
53. Wang, X.; Cheung, H.Y.M.; Chen, X.; Lam, L.Y.F.; Lo, I.M.C. Efficient peracetic acid activation by iron boride@biochar for pharmaceutical degradation and bacteria disinfection: Sustainable Fe(II) regeneration triggered by triple active sites. *Sep. Purif. Technol.* **2026**, *382*, 135633. [CrossRef]
54. Liu, J.; Zhu, J.; Gao, Q.; Zeng, X.; Zeng, Q.; Xiong, J.; Zhang, G.; Niu, Y.; Xie, H. Accelerate degradation of tetracycline via persulfate activation over S,N-Fe co-doped banana peel biochar: The role of pyrolysis temperature and $^1O_2$ evolution. *Chem. Eng. J.* **2025**, *509*, 161425. [CrossRef]
55. Liu, Y.; Liu, S.; Chen, M.; Bai, Y.; Liu, Y.; Mei, J.; Lai, B. Enhanced TC degradation by persulfate activation with carbon-coated CuFe2O4: The radical and non-radical co-dominant mechanism, DFT calculations and toxicity evaluation. *J. Hazard. Mater.* **2024**, *461*, 132417. [CrossRef] [PubMed]
56. Saravanakumar, K.; Jagan, G.; Njaramba, L.K.; Yoon, Y.; Park, C.M. Efficient photo-assisted activation of peroxydisulfate by a novel Z-scheme sulfur-doped C_3N_5/$DyFeO_3$ heterojunction for norfloxacin degradation: Activation mechanism and DFT studies on reaction pathways. *Environ. Res.* **2025**, *268*, 120735. [CrossRef]

57. Liu, W.; Yang, Y.; Li, Y.; Zhou, Y.; Wang, C.; Zhou, Y.; Shang, J.; Cheng, X. Oxygen vacancies enhanced natural manganese sand activation by PMS for CBZ degradation: Intermediate toxicity and DFT calculations. *Sep. Purif. Technol.* **2024**, *329*, 125015. [CrossRef]
58. Chen, Z.; Guo, J.; Kuang, Z.; Chen, W.; Yang, Y.; Zhou, Q. Accordion-like MXene-supported $CuFe_2O_4$ actuates persulfate activation for enhanced atrazine degradation: Radical mechanism, DFT calculations and potential toxicity evaluation. *Chem. Eng. J.* **2024**, *500*, 157179. [CrossRef]
59. Duan, X.; Yang, J.; Zhu, J.; Li, H.; Fang, Y.; Liu, R.; Yang, C.; Liu, W.; Ding, C.; Liu, Q.; et al. Activated CdS/sulfur doped g-C3N4 photocatalyst for dye and antibiotic degradation: Experimental and DFT verification of S-scheme heterojunction. *Environ. Res.* **2025**, *266*, 120487. [CrossRef]
60. Zhou, Y.; Tang, Z.; Zhao, X.; Wu, F.; Xie, F.; Zhao, T.; Da, C.; Liu, J.; Yang, X.; Li, J.; et al. Enhanced degradation of ofloxacin by novel zero-valent iron particles@V2C MXene composites with efficient activation of peroxomonosulfate: Mechanistic insights and DFT calculations. *Chem. Eng. J.* **2025**, *504*, 158893. [CrossRef]
61. Zhang, H.; Li, J.; Liu, Y.; Fu, S.; Su, T.; Meng, L.; Wang, Y.; Ma, N.; Liu, G.; Yan, Q.; et al. Sunlight-driven hydrogen peroxide activation via copper hydroxyphosphate with broad spectrum response for imidacloprid degradation: Mechanism insight and DFT calculation. *Chem. Eng. J.* **2025**, *521*, 166909. [CrossRef]
62. Lv, X.; Shu, A.; Shu, L.; Liu, H.; Liu, Y.; Cui, K.; Tang, Y.; Chen, X. Electron cycling mechanism in Fe/Mn DSAzyme accelerates BPA degradation and nanoenzyme regeneration. *J. Hazard. Mater.* **2024**, *476*, 135228. [CrossRef]
63. Fischer, J.; Kappelmeyer, U.; Kastner, M.; Schauer, F.; Heipieper, H.J. The degradation of bisphenol A by the newly isolated bacterium Cupriavidus basilensis JF1 can be enhanced by biostimulation with phenol. *Int. Biodeterior. Biodegrad.* **2010**, *64*, 324–330. [CrossRef]
64. Zheng, J.; Monfort, O.; Xu, J.; Shan, Y.; Ding, Q.; Wu, Y.; Dong, W. A novel CuS/persulfate/percarbonate dual-oxidant process for synergistic degradation of BPA: Crucial role of CO_3^{2-}. *Process Saf. Environ. Prot.* **2025**, *198*, 107116. [CrossRef]
65. Xu, P.; Li, N.; Ma, J.; Yao, J.; Hou, B. Performance and mechanism of tetracycline degradation by $CuCo_2O_4$ nanomaterial activated periodate. *Environ. Pollut.* **2025**, *378*, 126506. [CrossRef]
66. Zhang, N.; Wu, H.; Mao, Y.; Zhao, H.; Li, J. Nonradical peroxymonosulfate activation via high-level pyrrolic-nitrogen and electron-deficient carbon at 2D ultrathin carbonaceous nanosheets for efficient BPA removal. *J. Environ. Chem. Eng.* **2024**, *12*, 113877. [CrossRef]
67. Zeng, C.; Tan, G.; Zhang, B.; Guo, L.; Wu, X.; Fan, S.; Liu, W.; Wang, M.; Xia, A.; Ren, H.; et al. Piezoelectric-photothermal catalytic degradation of BPA by $Cs_{0.32}WO_3$ nanorods in dark-full spectrum. *J. Environ. Chem. Eng.* **2025**, *13*, 116058. [CrossRef]
68. Zhang, X.; Verbist, M.; Kamali, M.; Xue, Y.; Liu, Y.; Jin, P.; Costa, M.E.V.; Appels, L.; Cabooter, D.; Dewil, R. Activation of periodate with pinewood biochar-CuO composite for the removal of recalcitrant organic pollutants—Mechanisms and degradation products. *Chem. Eng. J.* **2023**, *465*, 142916. [CrossRef]
69. Zhuo, S.-N.; Zhang, W.; Ren, H.-Y.; Liu, B.-F. Highly efficient degradation of acetaminophen via nano zero-valent iron biochar with periodate system at low temperature. *Bioresour. Technol.* **2024**, *395*, 130349. [CrossRef] [PubMed]
70. Xu, J.; Wang, L.; Zhu, Y. Decontamination of Bisphenol A from Aqueous Solution by Graphene Adsorption. *Langmuir* **2012**, *28*, 8418–8425. [CrossRef]
71. Li, X.; Cheng, H. Crucial role of in-situ formed Mn(III) species in pollutant degradation by persulfate activated with Fe-Mn binary oxide-modified biochar. *Water Res.* **2026**, *295*, 125567. [CrossRef]
72. Shan, Y.; Song, B.; Ku, G.; Wang, L.; Wang, Z.; Chen, C.; Oladoja, N.A.; Ali, J.; Glebov, E.M.; Zhuang, X. Dual-pathway catalysis: Nano Fe-modified Platanus fluff biochar mediates peroxymonosulfate activation for enhanced tetracycline hydrochloride degradation through radical and non-radical synergies. *J. Environ. Chem. Eng.* **2026**, *14*, 122541. [CrossRef]
73. Zhang, X.; Cai, Z.; Liu, F.; Jiao, Y.; Zhang, M.; Peng, Q.; Wan, L. In situ assembly of Cu/N dual active sites on biochar via a metal ionic liquid for nonradical peroxydisulfate activation and efficient tetracycline degradation. *Chem. Eng. J.* **2026**, *537*, 176473. [CrossRef]
74. Yu, Y.; Xu, Q.; Wu, M.; Pang, Y.; Zhou, Y. Synergistic electro-activation of persulfate by boron-nitrogen co-doped sludge biochar for sulfamethoxazole degradation. *Sep. Purif. Technol.* **2026**, *400*, 138248. [CrossRef]
75. Wu, J.; Wang, Y.; Bai, J.; Li, X.; Gao, Y.; Li, G.; Zheng, Y.; Huo, M.; Wang, X. Cu_2O-modified magnetic iron-nitrogen co-doped biochar effective peroxymonosulfate activation for degradation of phthalate esters in reclaimed water. *Environ. Res.* **2026**, *302*, 124635. [CrossRef]
76. Liu, Y.; Cao, Y.; Sun, G.; Zhou, Z.; Li, X.; Chen, Z. Radical-driven peroxydisulfate activation by Fe–Mn bimetallic N-doped biochar for fluoxetine defluorination and degradation: Mechanistic insights and toxicity evolution. *J. Environ. Chem. Eng.* **2026**, *14*, 122891. [CrossRef]

77. Chandola, D.; Veres, B.; Varga, G.; Szamosvölgyi, Á.; Páli, T.L.; Sebők-Nagy, K.; Kozma, G.; László, Z.; Kónya, Z.; Alapi, T. Activation of peroxymonosulfate using biochar for the removal of trimethoprim: Effect of ball milling on catalytic efficiency, degradation pathway, and the contribution of the radical and non-radical processes. *J. Water Process. Eng.* **2025**, *81*, 109371. [CrossRef]
78. Yu, Y.; Chen, X.; Zheng, D.; Li, Y.; Chen, Z.; Chen, R.; Yang, L. New insights into enhanced catalytic degradation of sulfamethoxazole using Fe-Zn@biochar composite-activated periodate system: The combination of radical and non-radical pathways. *Colloids Surf. A Physicochem. Eng. Asp.* **2025**, *721*, 137265. [CrossRef]